1-1-2017

Electrolyte Interactions with Colloidal Gold Nanoparticles in Water

HA Ganganath Sanjeewa Perera

Electrolyte interactions with colloidal gold nanoparticles in water

By

H.A. Ganganath Sanjeewa Perera

A Dissertation
Submitted to the Faculty of
Mississippi State University
in Partial Fulfillment of the Requirements
for the Degree of Doctor of Philosophy
in Chemistry
in the Department of Chemistry

Mississippi State, Mississippi

August 2017

Electrolyte interactions with colloidal gold nanoparticles in water

By

H.A. Ganganath Sanjeewa Perera

Approved:

_____

Dongmao Zhang
(Major Professor)

_____

David O. Wipf
(Committee Member)

_____

Todd E. Mlsna
(Committee Member)

_____

Stephen C. Foster
(Committee Member)

_____

Joseph P. Emerson
(Graduate Coordinator / Committee Member)

_____

Rick Travis
Interim Dean
College of Arts & Sciences

Name: H.A. Ganganath Sanjeewa Perera

Date of Degree: August 11, 2017

Institution: Mississippi State University

Major Field: Chemistry

Major Professor: Dongmao Zhang

Title of Study: Electrolyte interactions with colloidal gold nanoparticles in water

Pages in Study 93

Candidate for Degree of Doctor of Philosophy

Electrolyte interactions with colloidal nanoparticles (NPs) in aqueous solutions have been implicated in a wide range of research and applications. Existing studies on electrolyte interactions with NPs are primarily based on the electrical double layer (EDL) theory. However, the EDL model provides very limited information on how electrolytes directly bind to NPs, electrolyte impact on charge distribution on NPs, and NP morphological modification upon electrolyte binding. Furthermore, the previous reports have mainly focused on either cations or anions binding onto NPs, while the potential cation and anion coadsorption onto NPs and NP-facilitated cation-anion interactions remain largely uncharted. Filling these knowledge gaps are critical to enhance the fundamental understanding of interfacial interactions of electrolytes with NPs.

Experimental characterization of cations and anions at the solid/liquid interface is a challenging analytical task. In the first study, we demonstrated the first direct experimental evidence of ion pairing on gold nanoparticles (AuNPs) in water by using surface enhanced Raman spectroscopy (SERS) in combination with electrolyte washing. Unlike ion pairing in aqueous solutions where the oppositely charged ions are either in direct contact or separated by a solvation shell, the ion pairing on AuNPs refers to cation

and anion coadsorption onto the same NP surface regardless of separation distance. Ion pairing reduces the electrolyte threshold concentration in inducing AuNP aggregation and enhances the competitiveness of electrolyte over neutral molecules in binding to AuNPs.

In the second study, we demonstrated that binding, structure, and properties of an ionic species on AuNPs are significantly dependent on the counterion adsorbed on AuNPs. These counterion effects include electrolyte-induced AuNP aggregation and fusion, quantitative cation and anion coadsorption on AuNPs, and SERS spectral distortion induced by the ionic species on AuNP surfaces.

In the final study, we proposed that ion pairing as the main mechanism for reducing electrostatic repulsion among organothiolates self-assembled on AuNPs in water by using a series of experimental and computational studies. The work described in this dissertation provides a series of new insights into electrolyte interfacial interactions with AuNPs.

DEDICATION

I would like to dedicate this doctoral dissertation to the Noble Triple Gem, my parents, Noel Perera and Thilakamali Perera, and my brothers, Chanaka Perera and Kasun Perera.

ACKNOWLEDGEMENTS

This dissertation would not be possible without the help and support of many wonderful people.

First and foremost, I would like to express my deepest gratitude to my advisor, Dr. Dongmao Zhang, for his valuable advice, encouragement, and support throughout this research.

I am grateful to my committee members Dr. David O. Wipf, Dr. Todd E. Mlsna, Dr. Stephen C. Foster, and Dr. Joseph P. Emerson for their helpful suggestions and discussions.

I want to thank all our collaborators: Dr. Shengli Zou (University of Central Florida), Dr. Felio Perez (University of Memphis), Dr. Maodu Chen (Dalian University of Technology), Dr. Gang Yang (Southwest University), Dr. T. Keith Hollis (Mississippi State University), and Dr. Charles U. Pittman, Jr. (Mississippi State University). I thank them all for their insightful input and valuable discussions.

I take this opportunity to thank my current and past lab members including Dr. Karthikeshwar Vangala, Dr. Siyam Ansar, Dr. Fathima Ameer, Dr. Manuel Gadogbe, Dr. Charles Nettles, Kumudu Siriwardana, Sumudu Athukorale, Buddhini Vithanage, and all my friends.

Finally, my most heartfelt acknowledgement goes to my family for their devotion, love, and support which helped me complete this research study successfully.

TABLE OF CONTENTS

LIST OF FIGURES

LIST OF ABBREVIATIONS

NPs	Nanoparticles
AuNPs	Gold nanoparticles
SERS	Surface enhanced Raman spectroscopy
SAM	Self-assembled monolayer
EDL	Electrical double layer
XPS	X-ray photoelectron spectroscopy
ICP-MS	Inductively coupled plasma-mass spectroscopy
TEM	Transmission electron microscopy
SEM	Scanning electron microscopy
FTIR	Fourier transform infrared spectroscopy
UV-vis	Ultraviolet-visible
LSPR	Localized surface plasmon resonance
CE	Chemical enhancement
EM	Electromagnetic enhancement
2-MBI	2-Mercaptobenzimidazole
ET	Ethanethiol
EDT	Ethanedithiol
BuT	Butanethiol
DBDS	Dibutyldisulfide

$(BBIB)X_2$	1,3-Bis(3'-butylimidazolium)benzene dihalide
(AM)X	1-Allyl-3-methylimidazolium halide
AME	Alkali metal electrolyte
MX	Metal halide
$(AuNP)_{sup}$	Gold nanoparticle supernatant

CHAPTER I

INTRODUCTION

The study of objects, materials, structures, and phenomena that have at least one dimension with a 1-100 nm regime is called nanoscience. Among different objects and systems studied in nanoscience, noble metal nanoparticles (NPs) have gained significant attention during the last five decades because of their critical contributions in numerous disciplines such as biosensing, drug delivery, catalysis, solar energy harvesting, and spectroscopy.[1-9] At the nanoscale regime, noble metal NPs exhibit interesting physical and chemical properties which are different from their bulk counter-parts. For example, gold nanoparticles (AuNPs) have a color of red or purple while bulk gold is a yellowish color.[10] Also, AuNPs are much more catalytically active while bulk gold is inert.[10]

Among the plethora of NPs studied to-date, AuNPs are the most extensively researched due to their unique physicochemical properties.[10-12] One of the key properties of AuNPs which has attracted significant attention is the ability to synthesize highly monodispersed AuNPs with controlled size and shape. AuNPs are commonly synthesized by the citrate-reduction method, which was first introduced by Turkevich in 1951.[13] In this method, chloroaurate ($AuCl_4^-$) is reduced by sodium citrate in water to produce spherical AuNPs with a diameter less than 100 nm. In this synthesis, citrate ions act as a reducing agent as well as a stabilizing agent of AuNPs. The negatively charged citrate ions are adsorbed onto AuNPs and the electrostatic repulsions among AuNPs imbue

AuNP dispersion stability in water. In 1973, AuNPs with a size range of 12-150 nm were synthesized by Frens, by varying the concentration ratio of $AuCl_4^-$ to citrate.[14] Another method of AuNP synthesis is the Brust-Schiffrin method.[15] In this method, $AuCl_4^-$ is reduced by sodium borohydride and the AuNPs are capped by a thiol. By using the Brust-Schiffrin method, only AuNPs with smaller sizes (1-3 nm) can be synthesized.

Surface modification of NPs with a variety of ligands is a common strategy to enhance the properties of NPs such as functionality, stability, and target specificity. The fundamental understanding of interfacial ligand interactions with NPs is extremely important to broadening the applications of NPs into different directions.

1.1 Interfacial ligand interactions with AuNPs

Surface functionalization of AuNPs with different ligands can tune the interfacial properties of AuNPs. The spontaneous adsorption of ligands onto AuNPs can form self-assembled monolayers (SAM), which are very useful in expanding the utilities of AuNPs.[16,17]

The surface functionalization of AuNPs can be performed by three main approaches. First, the AuNPs can be functionalized with ligands during AuNP synthesis. The synthesis of thiol functionalized AuNPs in the Brust-Schiffrin method is an example of the first approach.[15] The second approach is to functionalize the AuNPs after synthesis. Here, the incoming ligands are required to have a higher binding affinity than the ligands that are already adsorbed on the AuNP surface. As an example, the citrate-capped AuNPs can easily be functionalized with thiols, which displace the citrate molecules from the AuNP surface.[17,18] The third method is specific adsorption of an incoming ligand with a ligand that is already bound to the AuNP surface.[19]

Among a wide variety of ligands that have been used to functionalize AuNPs, this dissertation mainly focuses on studying the interfacial interactions of electrolytes and organothiols with AuNPs in water.

Amidst a range of electrolytes, alkali metal halides are the most common electrolytes that have been widely used to study interfacial interactions of AuNPs. As an example, KCl and NaCl are commonly used to induce AuNP aggregation especially for SERS spectral acquisitions.[20] Iodide and bromide ion-induced AuNP fusion is well known.[21,22] In one of our previous studies we demonstrated that iodide ions can rapidly reduce the SERS intensity of organothiols adsorbed on AuNPs through both iodide-induced organothiol desorption and AuNP fusion.[23] Halide ions are also important as shape-directing agents to synthesize gold nanostructures such as nanorods, nanoprisms, nanostars, and nanotriangles.[24-28] In recent years, sponge-like gold materials with nanosized pores which were fabricated using halides via a bottom-up approach[29] have gained increasing interest due to relatively large surface to volume ratio for applications in fuel cells, biosensors, and catalysts.[30-32] Iodide-induced gold dissolution is another example of halide-gold interactions.[33]

In addition to halides, nitrates, borohydrides, and sulfides are also utilized as electrolytes to study the interfacial interactions of AuNPs. As an example, Mirkin et al. reported the AuNP-based colorimetric determination of nitrate.[34] Ansar et al. successfully demonstrated sodium borohydride-induced (1) displacement of ligands such as organothiols, halides, dyes, and polymers from AuNP surfaces[35] and (2) desulfurization of thioamides on AuNPs.[36] Sodium borohydride is also important in AuNP synthesis[15]

and assembling AuNPs into chainlike structures.[37] Zhang et al. reported that sulfide ions can be used as an anti-aggregating agent of AuNPs.[38]

Along with electrolytes, organothiols, organic molecules with thiol functional groups, have also been widely used to functionalize AuNPs.[16] The ability of organothiols to bind onto AuNPs via strong Au-thiolate covalent bonds (~50 kcal/mol) has caused organothiols to attract significant attention in functionalizing AuNPs.[39] The adsorption of organothiols onto AuNPs is spontaneous and form SAMs over a relatively short period of time (from a few seconds to minutes). The organothiol adsorption kinetics, surface coverage, and binding structure on AuNPs can be altered by factors such as organothiol concentration, solvent, temperature, incubation time, organothiol purity, and organothiol chain length.[40-43]

The next section discusses different analytical techniques used to characterize the surface chemistry of the electrolytes- and organothiols-interacted AuNPs.

1.2 Analytical techniques for studying ligand interactions with AuNPs

Surface analytical techniques are extremely important to comprehensively understand the nanoparticle surface chemistry. Therefore, choosing the correct analytical tool is critical in studying ligand interactions with AuNPs. However, characterization and quantification of ligand functionalized AuNPs are very challenging, mainly due to the extremely low amount of ligands adsorbed onto the AuNPs. The analytical tool used should be sensitive to detect these ligands and be selective to differentiate the ligand from the background and other competing agents in order to derive meaningful conclusions.

The main spectroscopic tool used to characterize electrolyte-induced AuNP aggregation is UV-vis spectroscopy.[29] The red shifting and broadening of the localized

surface plasmon resonance (LSPR) peak of the AuNPs in the UV-vis spectrum after the addition of an electrolyte is a clear indication of AuNP aggregation. AuNPs can strongly interact with light. The LSPR of AuNPs occurs when the collective oscillations of the conduction band electrons are equal to the frequency of the incident light.[44] As a result, a strong extinction is exhibited for AuNPs in UV-vis spectrum. Schematic representation of the LSPR of spherical NPs is shown in Figure 1.1. The LSPR of a NP depends on factors such as size, shape, dielectric environment, and the aggregation state of NPs.[45-48]

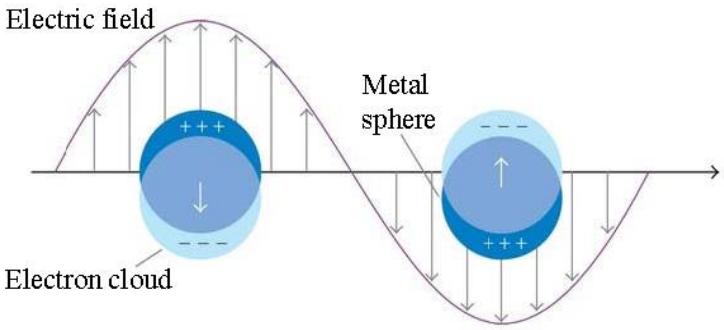

Figure 1.1 Schematic representation of plasmon oscillation of spherical NPs. Reproduced with permission from ref 46. Copyright 2007 Annual Reviews.

The electrolyte-induced morphological changes of AuNPs are mainly characterized by using scanning electron microscopy (SEM) and transmission electron microscopy (TEM).[21,22,29] The surface charge of the AuNPs after interacting with electrolytes is mainly characterized by zeta potential (ξ) measurements.[49] ξ is a key parameter when judging AuNP stability in a solution. Energy dispersive X-ray spectroscopy (EDX) is commonly used for qualitative and quantitative measurements of the electrolytes on AuNPs.[22] X-ray photoelectron spectroscopy (XPS) is also an

important technique to characterize the elemental composition and the charge state of electrolytes on AuNPs.[24]

Organothiol adsorption and structure on AuNPs have been characterized by using a wide range of analytical methods such as Fourier transform infrared spectroscopy (FTIR),[50,51] XPS,[52,53] nuclear magnetic resonance spectroscopy (NMR),[54,55] and surface enhanced Raman spectroscopy (SERS).[41,56,57]

The main analytical tool use to study the work described in this dissertation is SERS. The following section provides information about the fundamental principles governing the SERS phenomenon.

1.3 Surface enhanced Raman spectroscopy (SERS)

The direct sensitive detection of analytes in Raman spectroscopy is difficult due to the low inelastic scattering efficiency of photons. In contrast, in the presence of a metal surfaces, the same analyte produces a strong Raman signal with signal enhancements as high as 10^6-10^8 in magnitude.[58-60] Since the signal of the molecule is enhanced by many orders of magnitude in the presence of a metal surface, this spectroscopic method is called surface enhanced Raman spectroscopy (SERS). Since its discovery in the 1970s, SERS has become a highly useful analytical tool to study ligand adsorption onto NPs due to advantages such as single molecule detection sensitivity, the ability to obtain spectra in aqueous media, and fingerprint spectra of the molecules.[61-63]

Two main mechanisms have been proposed for the signal enhancement in SERS measurements. They are chemical enhancement (CE) and electromagnetic enhancement (EM). It is proposed that the CE in SERS occurs mainly due to charge transfer interactions between the molecule and the metal nanoparticle. The contribution to the

magnitude of the SERS signal by CE is typically ~10^2.[64,65] In EM, the incident electromagnetic field resonates with the surface plasmons of metal NPs and the Raman signal is enhanced. In contrast to CE, EM contributes more than 10^4 enhancement of the Raman signal intensity.[66,67] The relationship between the applied electric field (E_0) and the electromagnetic field induced ($E_{induced}$) on the surface of a spherical NP is given by Eq.1.1.[68]

$$E_{induced} = [\frac{\varepsilon_1(\omega) - \varepsilon_2}{\varepsilon_1(\omega) + 2\varepsilon_2}]E_0 \quad (1.1)$$

Where;

$\varepsilon_1(\omega)$ - frequency dependent dielectric function of the metal

ε_2 - relative permittivity of ambient phase

It is well-established that the SERS signal can further be enhanced by reducing the gap between the NPs.[69,70] As the gap between NPs is reduced, the EM enhancement is integrated over the entire NP surface and the molecules located at these gaps experience an enhanced electric field leading to an enhanced signal.[71,72] The reduction of the gap between NPs are commonly achieved by NP aggregation which occurs by either spontaneous self-assembly of ligands on NPs or by the addition of aggregating electrolytes such as KCl and KNO_3.[73]

Besides the SERS signal enhancement, NP aggregation raises new questions such as what is the threshold concentration of the electrolyte to induce NP aggregation, what forces stabilize the NPs, what is the mechanism for NP aggregation, and does the NP aggregation depend on the electrolyte. The following sections will discuss the proposed

mechanisms for the stability of dispersed NPs. Since the main focus of this dissertation is citrate-reduced AuNPs, the subjected mechanisms will be discussed with reference to citrate-reduced AuNPs.

1.4 Electrical double layer (EDL) theory

With the well-established electrical double layer (EDL) theory for the charge distribution on planar metal surfaces in a solution,[74-77] it is widely accepted that citrate-reduced AuNPs are stabilized by a double layer of opposite charges.[78,79] The negatively charged citrate ions are directly adsorbed onto the AuNP surface while the counter cations are located in the diffuse layer to reduce the electrostatic repulsions among citrate anions on the same AuNP. In a typical citrate-reduced AuNP solution, the electrostatic repulsions among the negatively charged AuNPs are stronger than the intermolecular van der Waals attractions. Therefore, AuNPs are highly dispersed and stabilize in water. The EDL theory is also used to explain the stability of the densely packed thiolated AuNPs in which the counter cations are located in the diffuse layer to reduce the electrostatic repulsions among negatively charged thiolates. The charge distribution of citrate-capped AuNPs in an aqueous solution according to the EDL theory is shown in Figure 1.2.

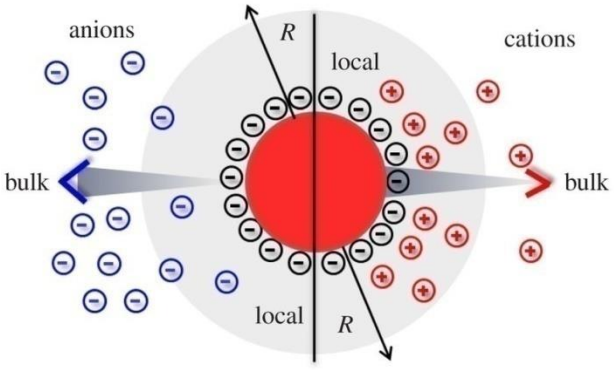

Figure 1.2 Schematic representation of ionic species distribution of citrate-reduced AuNPs in water, according to the EDL theory.

Reproduced with permission from ref 78. Copyright 2014 The Royal Society.

The thickness of the diffuse layer is highly dependent on the ionic strength of the solution. With the addition of an electrolyte, the ionic strength of the solution is increased. The Debye screening length of the particles, which is the measure of the thickness of the electrical double layer of charged particle in solution, decreases with increasing electrolyte concentrations.[78,80] The DLVO (Derjaguin, Landau, Verwey, and Overbeek) theory stipulates that with increasing solution ionic strength, the Debye screening length can be reduced to a degree that the interparticle van der Waals interaction eventually overcomes the electrostatic repulsion between the colloidal particles of the same charge, leading to NP aggregation.[81]

While the EDL theory is consistent with the general experimental observations that colloidal AuNPs have poor dispersion stability in solutions with high electrolyte concentrations, it cannot explain the specific ion effects in which some of the electrolytes are drastically more effective than others in inducing AuNP aggregations. Additionally, an alternative explanation is required for the ability of negatively charged organothiols to

densely pack on AuNPs by overcoming electrostatic repulsions. Ion pairing, coadsorption of anions and cations on AuNPs, can serve as an alternative mechanism for explaining these phenomena.

1.5 Ion pairing

The association of oppositely charged ionic species can be generally called ion pairing and usually this refers to the ion pairs in solution. Ion paring has a significant effect on the structural and physiochemical properties of a range of chemical and biological systems such as in ion exchange chromatographic separations and protein folding.[82-84] Typically there are two types of ion pairing systems found in solution. They are (1) solvent separated- and (2) contact-ion pairing. The solvent separated ion pairing is further categorized based on whether the same solvent molecule is shared by the two ionic species or not (Figure 1.3).[82,85]

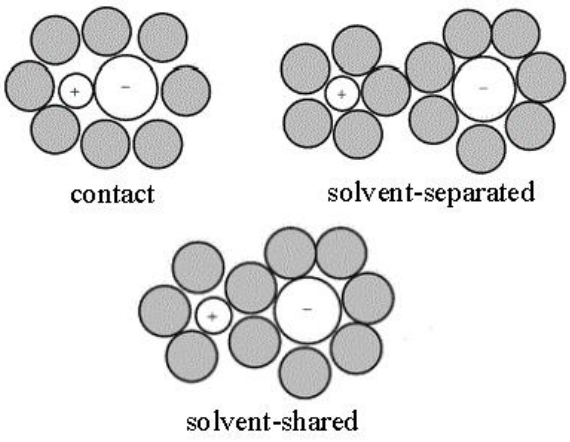

Figure 1.3 Schematic representation of different types of ion pairs in solution. Reproduced with permission from ref 85. Copyright 2009 Royal Society of Chemistry.

In solvent separated ion pairing, the two oppositely charged ions are separated by the solvent molecules. In solvent shared ion pairing, the same solvent molecule is shared by both oppositely charged ions. In contact ion pairing, positive and negative ions are in direct contact with each other. The ion pairing at liquid/solid interfaces is different from the ion pairing in solution. Furthermore, unlike ion pairing in solution, the direct observation of ion pairing at the liquid/solid interface is challenging. These challenges and the direct observation of ion pairing on AuNPs will be discussed in detail in Chapter II.

1.6 Dissertation objectives

Electrolyte and organothiol interactions with colloidal AuNPs have broad implication to a wide range of scientific and technological applications. Deepening the fundamental understanding of these interactions is extremely critical to expand the utility of AuNPs toward different directions. The key objectives of this dissertation are (1) to offer direct experimental evidence of ion pairing on AuNPs, (2) investigation of the effects of different anions and cations binding on physicochemical properties of AuNPs, and (3) elucidation of the mechanism of the stability of organothiolates self-assembled on AuNPs.

This dissertation is composed of four related chapters. Chapter I of this dissertation serves with an overview of the current state-of-knowledge of the subjects related to the dissertation. Chapter II discusses the first direct experimental evidence of ion pairing, the coadsorption of anions and cations onto AuNPs in water by using SERS measurements in combination with electrolyte washing experiments. The main focus of Chapter III is to study the counterion effects on electrolyte interactions with AuNPs in

water. The final chapter, Chapter IV, describes the mechanism of organothiol binding onto AuNPs in water by using simple pH measurements. This chapter further describes that ion pairing as the main pathway for reducing electrostatic repulsion among self-assembled organothiolates on AuNPs in water. The insights provided in these studies represent a significant step forward in the comprehensive understanding of electrolyte and organothiol interfacial interactions with colloidal AuNPs in water.

CHAPTER II

DIRECT OBSERVATION OF ION PAIRING AT THE LIQUID/SOLID INTERFACES BY SURFACE ENHANCED RAMAN SPECTROSCOPY

(Published in *Langmuir* **2015**, *31*, 8998-9005)

2.1 Abstract

Ion pairing, the association of oppositely charged ionic species in solution and at liquid/solid interfaces has been proposed as a key factor for a wide range of physical and chemical phenomena. However, experimental observations of ion pairing at the ligand/solid interfaces are challenging due to difficulties in differentiating ion species in the electrical double layer from that adsorbed on the solid surfaces. Using surface enhanced Raman spectroscopy in combination with electrolyte washing, we present herein the first direct experimental evidence of ion pairing, the coadsorption of oppositely charged ionic species onto gold nanoparticles (AuNPs). Ion pairing reduces the electrolyte concentration threshold for inducing AuNP aggregation and enhances the cooperativeness of electrolyte over neutral molecules for binding to AuNP surfaces.

2.2 Introduction

Ion pairing, the association of oppositely-charged ionic species has tremendous effect on the structure and phyical and chemical properties for a wide range of chemical and biological materials.[82,86,87] For example, ion pairing plays a critical role in protein folding, DNA conformational change, and ion exchange chromatographic

separations.[83,84,88] There are two types of ion pairing:[89] (1) contact ion pairing in which a positive and negative ion are in direct contact and (2) solvent separated ion pairing where the two oppositely charged ions are separated by solvent molecules such as water. There are extensive theoretical and experimental works on the fundamental understanding of the mechanism and the effect of ion pairing in aqueous solution,[90-92] both for ion pairing between ions dispersed in solution and at liquid/solid interfaces.[93-95] However, direct experimental observation has been observed only in concentrated solutions with small-angle X-ray scattering and NMR measurements,[84,92] while the ion pairing at liquid/solid interfaces has, to our knowledge, been deduced entirely from indirect experimental observations such as ion exchange separations. There are two key challenges in determining ion paring at liquid/solid interfaces. First, the amount of ionic species that can be directly adsorbed onto a solid support is likely limited, which imposes a sensitivity challenge to the employed analytical method. Second, the experimental strategy has to be able to differentiate the ionic species that are in diffuse electrical double layer (EDL) from that directly bounded to the solid surfaces. The latter can be especially challenging giving the fact that EDL is only a few nanometers in thickness.

Using surface enhanced Raman spectroscopy (SERS) in combination with electrolyte washing, we presented in this work direct experimental evidence of ion pairing, the coadsorption of anions and cations on gold nanoparticle (AuNP) surfaces, and its drastic effect on the competitive ligand adsorption and electrolyte-induced AuNP aggregation. SERS is an ultrasensitive analytical method that is highly selective for molecules that are directly adsorbed onto or in extremely close vicinity to the nanoparticle surface,[42,96,97] which the electrolyte washing experiment provides a simple

mean for us to determine whether ionic species observed in the SERS spectra are indeed directly adsorbed onto the AuNPs or in the diffuse layer. In analogy to what has been observed in ion exchange column, the ions in the EDL diffuse layer or loosely bound to the nanoparticle surfaces should be displaceable by ionic species in the washing electrolyte (Figure 2.1). Only the ionic species that are directly adsorbed onto AuNPs can remain adsorbed on the nanoparticle surfaces. It is noted that the term ion pairing in this work refers to the coadsorption of both cation and anion onto the AuNPs, regardless whether cations and anions are separated or collocated at the same positions on AuNP surfaces.

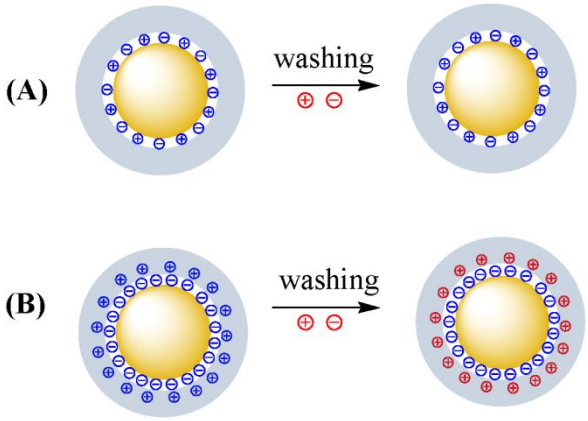

Figure 2.1 Effect of electrolyte washing on ionic species that (A) are strongly bounded to the AuNP surfaces and that (B) located in the diffuse EDL of the charge AuNP.

Note: Only ions that are directly adsorbed onto the AuNPs can remain bounded after electrolyte washing.

The model electrolytes used in this study include alkali metal halide salts (MX in which $M=K^+$, Na^+, and Li^+; $X=Cl^-$, Br^-, and I^-), 1,3-bis(3'-butylimidazolium)benzene dihalides salts ($(BBIB)X_2$ in which $X= Cl^-$, Br^-, and I^-), and five 1-allyl-3-

methylimidazolium (AM) halide salts in which the anions include Cl^-, Br^-, and I^-, dicyanamide, and bis(trifluoromethylsulfonyl)imide (Figure 2.2). We refer hereafter to three component-solutions as (A/B)/C in which the two components (A and B) inside the parenthesis are mixed first before mixing the addition of C.

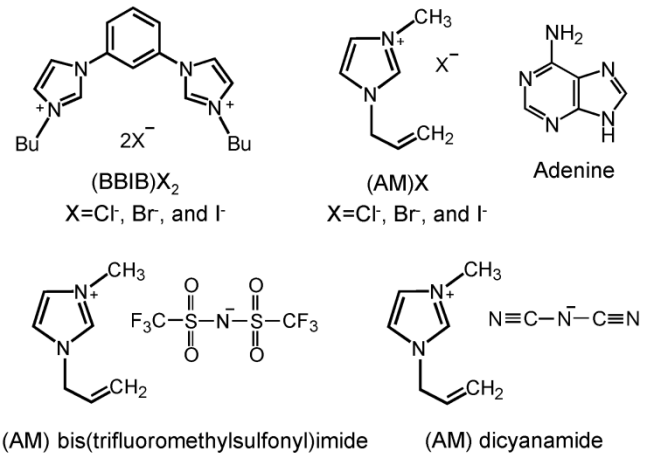

Figure 2.2 Molecular structures of the model electrolytes used in this study.

2.3 Experimental section

2.3.1 Materials and equipment

All chemicals were purchased from Sigma-Aldrich and used as received. $(BBIB)X_2$ salts were prepared in house with published procedure.[98] The SERS spectra were acquired using the LabRam ARAMIS confocal Raman microscope system with a 633 nm HeNe Raman excitation laser.

2.3.2 AuNP synthesis

AuNPs were synthesized using citrate reduction method.[14] In brief, $HAuCl_4.3H_2O$ (0.0415g) was added to 100 mL of 18 MΩ-cm Nanopure water, and the solution was

brought to boil. Then 10 mL of 1% trisodium citrate dehydrate was added, and the mixture was kept boiling for ~20 min while stirring. The average diameter of the AuNPs was determined to be ~13 nm (Figure 2.3). The concentration of as-synthesized AuNPs was determined to be ~13 nM on the basis of molar absorption coefficient of 13 nm AuNPs which is 2.7×10^{8} M^{-1} cm^{-1}.[99,100]

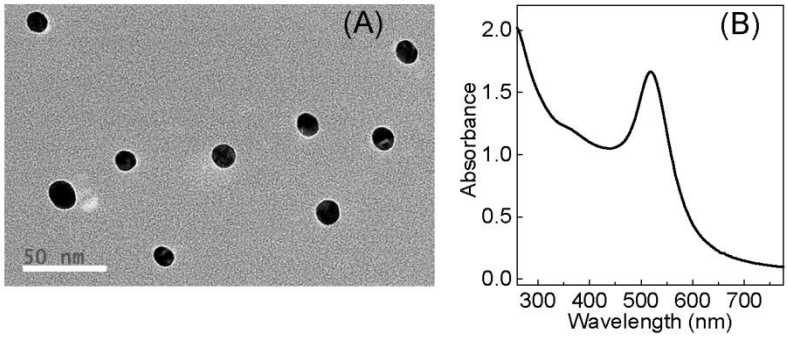

Figure 2.3 (A) TEM image of as-synthesized AuNPs and (B) UV-vis spectrum of 2.2 times diluted as-synthesized AuNPs used in this study.

2.3.3 SERS spectral acquisition

As-synthesized AuNPs were mixed with an equal volume of MX and $(BBIB)X_2$ with predefined concentrations. The AuNPs/ligand mixtures were allowed to incubate overnight for the aggregates to settle down. The SERS spectra were acquired after the AuNP aggregates were deposited on the stainless steel substrates. All the SERS measurements were conducted while the samples were wet. The spectral integration time was varied from 10-200 s with 10-50 accumulations. Spectra were acquired using ×10 objective and the laser power was 1.3 mW before objective.

2.3.4 KNO_3 washing experiment

SERS spectra were acquired for the overnight incubated MX/AuNPs and (BBIB)X_2/AuNPs aggregates. Then each aggregate was incubated with 1 mM KNO_3 for ~15 min and the supernatant was replaced with another fresh portion of 1 mM KNO_3. This procedure was conducted for ~ 10 times. Finally, each aggregate was incubated with 1 mM KNO_3 for overnight before acquiring the SERS spectrum.

2.3.5 Competitive adsorption of adenine with MX or (BBIB)X_2 onto AuNPs

An equal volume of specified concentrations of adenine and MX (or (BBIB)X_2) were mixed together and incubated for ~ 5 min. Then each mixture was added to an equal volume of AuNPs and allowed the aggregates to settle. SERS spectra were acquired after depositing the aggregates on a stainless-steel substrate.

2.3.6 Zeta potential measurements of the AuNPs

Equal volume of AuNPs was mixed with predefined concentrations of (BBIB)I_2 and KI, and allowed to react overnight. Zeta potential measurements were taken for these samples at 25˚C using a ZetaPALS analyzer (Brookhaven Instruments Corporation (BIC), Holtsville, NY). Phase Angle Light Scattering measurements were detected at a 90˚ angle while Electrophoresis Light Scattering measurements were acquired with the detector at 15˚ angle. After the sample was stabilized in the cuvette for 3 min, a total of 10 measurements were acquired for each sample.

2.3.7 Fluorescence quantification of $BBIB^{2+}$ adsorption onto AuNPs

Fluorescence measurements of AuNP/(BBIB)Cl_2 and $AuNP_{sup}$/(BBIB)Cl_2 were acquired with a Horiba JobinYvon FluoroMax-4 spectrofluorometer in 1 cm x 1 cm

cuvettes. The $(BBIB)Cl_2$ containing samples were excited at 252 nm and show an emission maximum at 315 nm. The resulting fluorescence signal of the supernatant of these solutions was resulted from $BBIB^{2+}$ remaining free in solution. A calibration plot $BBIB^{2+}$ fluorescence intensity at 315 nm as a function of $(BBIB)Cl_2$ concentration was acquired using $(BBIB)Cl_2$ concentrations of 0.1, 2, 5, 10, 20, and 30 μM dissolved in AuNP supernatant. This calibration plot allowed for quantification of the free $BBIB^{2+}$.The amount adsorbed onto AuNPs was calculated by subtraction of the free amount from the amount initially added. Centrifugation was conducted using a Fisher Scientific Marathon 20111R centrifuge at 9000 rpm for 75 min at 15 ^oC or until the AuNP LSPR peak (~520 nm) was no longer detectable in the supernatant.

2.3.8 Computational simulations

Gaussian 09 is used to optimize the structure of $(BBIB)^{2+}$, $(BBIB)Cl_2$, $(BBIB)Br_2$, and $(BBIB)I_2$. Since iodine atom is involved, we used the bp86 method with basis sets of DGDZVP for all the calculations where the model molecules are in water solution. The as-calculated Raman shifts were used to compare the computed Raman spectra and their experimental counterparts. No frequency scaling was performed. The computational simulations were performed by Dr. Shengli Zou in University of Central Florida.

2.4 Results and discussion

2.4.1 Electrolyte-induced AuNP aggregation

Electrolytes differ significantly in their threshold concentration to induce AuNP aggregations. Figure 2.4 shows the photograph and the SERS spectra obtained with AuNP/KX and AuNP/$(BBIB)X_2$. The minimum MX concentration leading to AuNP

aggregation is above 10 mM, while that for all tested $(BBIB)X_2$ (Figure 2.4) is 2 μM, over 5000 times lower than that for MX. These data indicate that organic-cation-containing electrolytes are far more effective than MX in inducing AuNP aggregation.

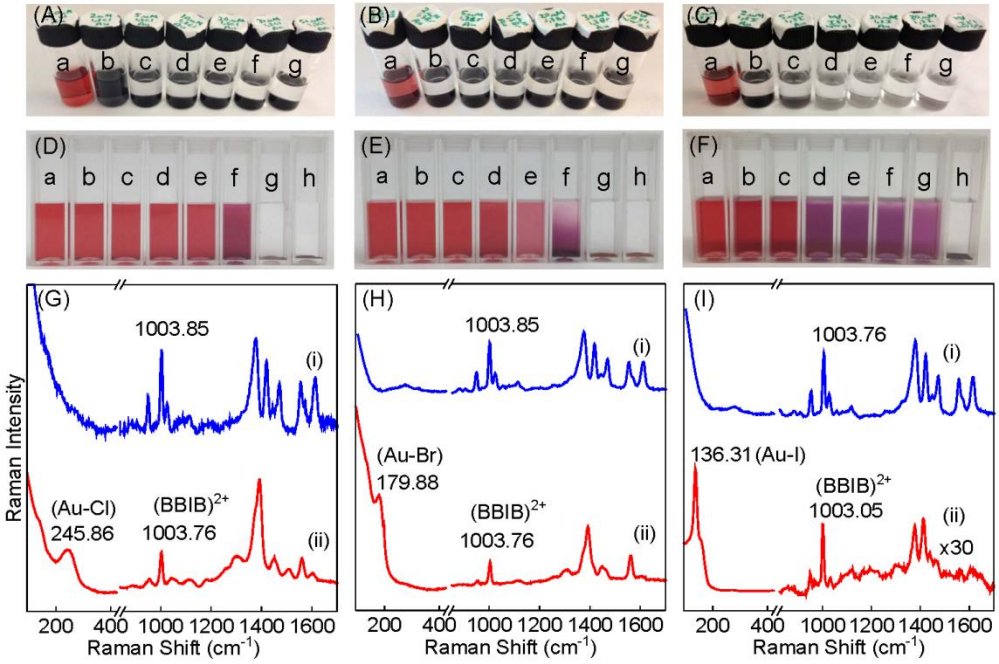

Figure 2.4 Photographs of the (A) AuNP/$(BBIB)Cl_2$, (B) AuNP/$(BBIB)Br_2$, (C) AuNP/$(BBIB)I_2$, (D) AuNP/KCl, (E) AuNP/KBr, and (F) AuNP/KI solutions. (G)-(I) are the (i) normal Raman and (ii) SERS spectra of $(BBIB)Cl_2$, $(BBIB)Br_2$, and $(BBIB)I_2$, respectively.

Note: The nominal concentrations of $(BBIB)X_2$ in (A)-(C) from (a)-(g) are 0, 2, 5, 10, 20, 30, and 50 μM, respectively. The nominal concentrations of KX in (D)-(F) from (a)-(h) are 0, 2, 5, 10, 20, 30, 40, and 50 mM, respectively. The nominal concentration of $(BBIB)X_2$ in normal Raman spectra in (i) of (G)-(I) is 20 mM. The nominal concentrations of AuNPs and $(BBIB)X_2$ in SERS spectra are 6.5 nM and 10 μM, respectively. The spectra in Figure (G)-(I) were normalized and offset for clarity. The number in spectrum (I)(ii) is the scaling factor for the spectral feature in the ~700 to 1650 cm^{-1} region in comparison to its spectral feature below 400 cm^{-1} region.

With similar to $(BBIB)X_2$, all $(AM)^+$ salts used in this study also induced AuNP aggregation when the $(AM)^+$ salt concentration is 2 μM (Figure 2.5).

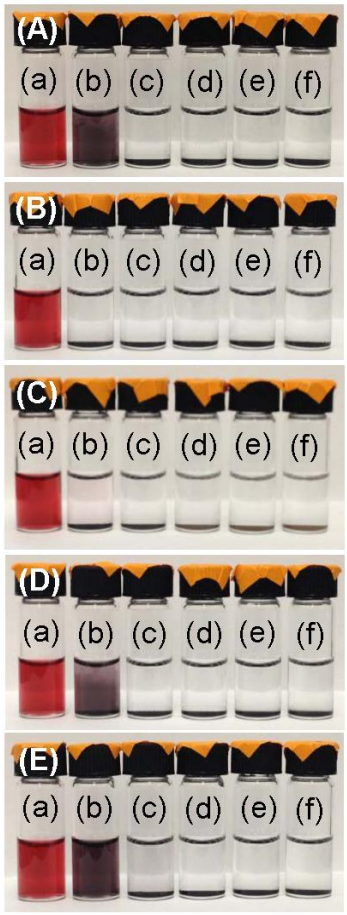

Figure 2.5 Photographs of (A) AuNPs/(AM)Cl, (B) AuNPs/(AM)Br, (C) AuNPs/(AM)I, (D) AuNPs/(AM) bis(trifluoromethylsulfonyl)imide, and (E) AuNPs/(AM) dicyanamide.

Note: The nominal concentrations of $(AM)^+$-salts are (a) 0, (b) 2, (c) 5, (d) 10, (e) 100, and (f) 500 μM. The nominal concentration of AuNPs is ~6.5 nM.

Zeta potential measurements conducted with KI and $(BBIB)I_2$ reveal that AuNPs mixed with $(BBIB)I_2$ have reduced the surface potential drastically (ξ>-12 mV) when the electrolyte concentration is ~2 μM, but to obtain a similar reduction in surface potential

for the same batch of AuNPs needs at least 12 mM KI (Figure 2.6). AuNPs in KI with concentration of 2 mM or below remains highly negatively charged (ξ<-30 mV) as in the as-synthesized AuNPs. This drastic difference between MX and its corresponding $(BBIB)^{2+}$- and $(AM)^{+}$-containing halide salts in their threshold concentrations for neutralizing AuNPs and inducing their aggregation cannot be readily explained by the EDL theory if one assumes that the charge-density on the as-synthesized AuNPs remains unchanged in the electrolyte-containing solution. Under this assumption, these electrolyte threshold concentrations for inducing AuNP aggregation should be much more similar according to the Smoluchowski equation.[80] Indeed, the low μM $(BBIB)^{2+}$- and $(AM)^{+}$-containing salts in this case would have negligible effect on the AuNP ξ potential because of the small Debye–Hückel parameter.[80]

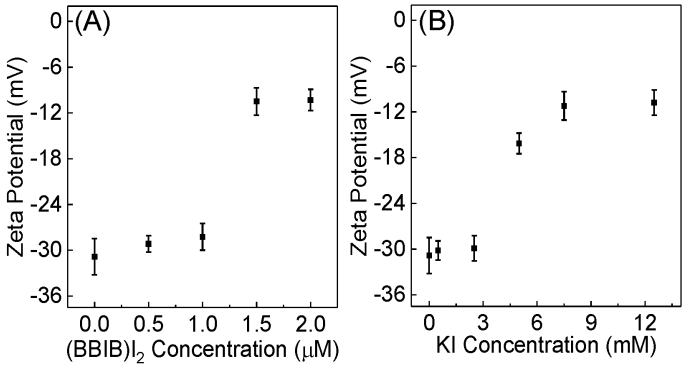

Figure 2.6 Variation of the zeta potentials for the AuNPs mixed with different concentrations of (A) $(BBIB)I_2$ and (B) KI.

Note: The nominal concentration of AuNPs was ~6.5 nM. The measurements were conducted within five hours of the sample preparation. The error bar represents of one standard deviation of the mean. It is noted that the AuNP zeta potentials for samples that contain 1.5 μM and 2 μM $(BBIB)I_2$, and that contains 7 mM and 13 mM KI should be treated as semi-quantitative. This is because there are notable AuNP aggregations in those samples. Therefore the measured charge zeta potentials are representative only for the AuNPs that may be aggregated but not settled.

Multiple experimental results indicate that ion pairing is the key driving force for the facile $(BBIB)X_2$- and (AM)X-induced AuNP aggregation. In case of AuNP/$(BBIB)X_2$, both $BBIB^{2+}$ and Au-X SERS features appeared in the SERS spectra obtained with all AuNP/$(BBIB)X_2$ samples (Figure 2.4).The $(BBIB)^{2+}$ SERS feature is identified by comparing the SERS spectra of AuNP/$(BBIB)X_2$ with the normal Raman spectra obtained with $(BBIB)X_2$ solution, while Au-X SERS peak is identified on the basis of literature Raman shifts reported for I-Au (130 cm^{-1} ~ 160 cm^{-1}),[101,102] Au-Br (170 cm^{-1} ~ 200 cm^{-1}),[103,104] and Au-Cl (240 cm^{-1} ~ 275 cm^{-1}).[105] The concurrent appearance of these cation and anion SERS features indicates that $BBIB^{2+}$ and X^- are directly attached, or in close vicinity to the AuNPs. This is because SERS is a near-field phenomenon,[61] only molecules that are in direct contact with the AuNP surface or within a few nanomaters from the AuNP surface can be detected with SERS.

2.4.2 Electrolyte washing experiment

The SERS-based electrolyte washing experiments demonstrate that both $(BBIB)^{2+}$ and X^- are in direct contact with the AuNPs (Figure 2.7). In washing experiments the $(BBIB)X_2$-containing AuNP aggregates prepared by mixing equal volume of 10 μM $(BBIB)X_2$ with as-synthesized AuNPs were washed extensively with 1 mM KNO_3. Both $(BBIB)^{2+}$ and X^{-1} features remain in the SERS spectra obtained with the overnight washed samples. These data provide direct evidence that $(BBIB)^{2+}$ and halide are coadsorbed on AuNPs. Otherwise, SERS signature of one ionic species should disappear in the washed samples. This cation and anion coadsorption explains why the ξ potential can be so drastically lower than the as-synthesized AuNPs even when the electrolyte concentration is at low micromolar range.

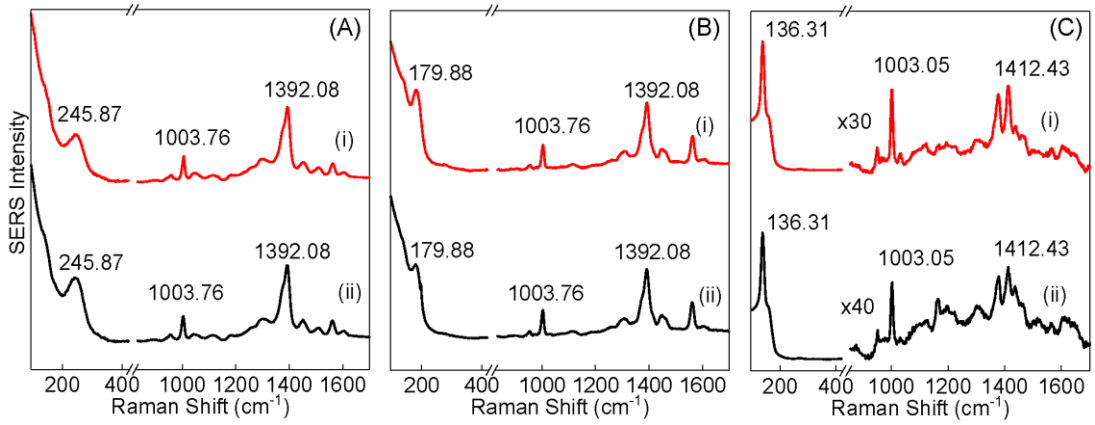

Figure 2.7 The SERS spectra of (A) AuNP/(BBIB)Cl_2, (B) AuNP/(BBIB)Br_2, and (C) AuNP/(BBIB)I_2 (i) before and (ii) after extensive washing with KNO_3.

Note: The spectra were normalized and offset for clarity. The number in spectrum (C) is the scaling factor for the spectral feature in the ~700 to 1650 cm^{-1} region in comparison to its spectral feature below 400 cm^{-1} region.

2.4.3 Computationally modeled $BBIB^{2+}$ Raman spectra

The experimental normal Raman spectra of all three $BBIB^{2+}$ halide salt solutions are highly identical (Figure 2.4). This result is expected since (BBIB)X_2 are electrolytes and the cations and anions are dissociated in solution. To facilitate the peak assignment the $BBIB^{2+}$ normal Raman and SERS spectra were compared with computationally modeled Raman spectra of $BBIB^{2+}$ (Figure 2.8). The computational normal Raman spectrum is highly similar to the experimental counterparts. The $BBIB^{2+}$ SERS peak correlations differ significantly from that observed in $BBIB^{2+}$ normal Raman spectra, and such differences varies as a function of the types of (BBIB)X_2 salts (Figure 2.8). However, one can find a corresponding normal Raman peak for all the SERS peaks observed in experimental (BBIB)X_2 SERS spectra. This result confirms the fidelity of the $BBIB^{2+}$ SERS spectra. The difference between the $BBIB^{2+}$ normal and SERS feature are due most likely to the fact that only a subset of Raman active modes in $BBIB^{2+}$ were

enhanced. The SERS differences among different SERS samples are due to change in $BBIB^{2+}$ molecular orientation on the AuNP surfaces. The degree of the SERS enhancement in the experiments by specific vibration modes depends both on not only the molecular orientation of the involved functional group,[106] but also its distance from the AuNP surfaces.

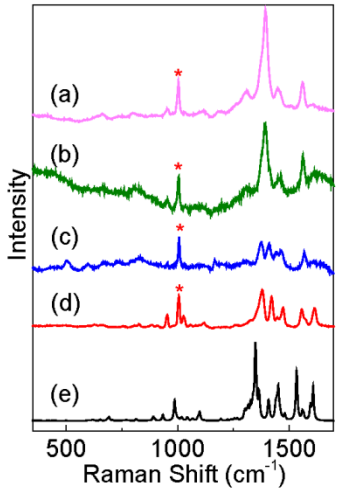

Figure 2.8 Experimental SERS spectra of (a) (AuNP/(BBIB)Cl_2, (b) (AuNP/(BBIB)Br_2, (c) (AuNP/(BBIB)I_2, (d) experimental normal Raman spectrum of $BBIB^{2+}$ of (BBIB)I_2, and (e) computationally modeled Raman spectrum of $BBIB^{2+}$.

Note: All the experimental spectra were normalized to the peak at 1003 cm^{-1}, denoted by '*'. The nominal concentrations of (BBIB)X_2 and AuNPs for SERS are 10 μM, and 6.5 nM, respectively. The nominal concentration of (BBIB)I_2 for normal Raman is 20 mM.

Despite the similarity of the experimental and computed Raman spectra, confident peak assignments are challenging. This is because $BBIB^{2+}$ contains 52 atoms and it has total of 150 fundamental vibrational modes. Essentially every vibrational mode involves multiple functional groups, and many observed Raman peaks involve several vibrational

modes. Therefore, only a few major peaks were tentatively assigned graphically in this work (Figure 2.9).

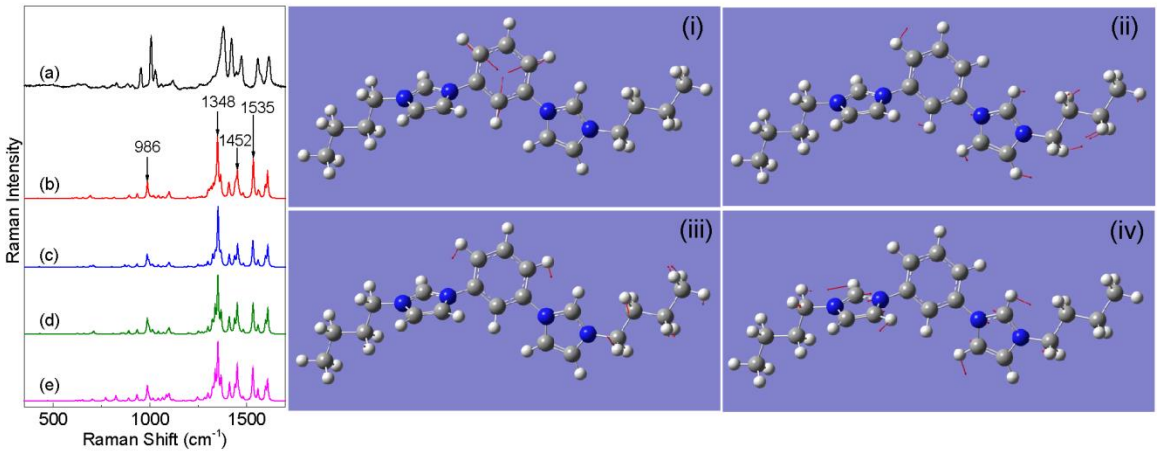

Figure 2.9 (a) Experimental normal Raman spectrum of $(BBIB)I_2$, computationally modeled normal Raman spectra of (b) $BBIB^{2+}$, (c) $(BBIB)Cl_2$, (d) $(BBIB)Br_2$, and (e) $(BBIB)I_2$.

Note: (i) to (iv) are the graphic representation of vibrational modes in the computed $BBIB^{2+}$ normal Raman spectra of the peaks at 986, 1348, 1452, and 1535 cm^{-1}, respectively.

2.4.4 Concentration dependence SERS spectra of $(BBIB)X_2$

The structure and composition of cations and anions coadsorbed onto AuNPs depends strongly on $(BBIB)X_2$ concentrations when the $(BBIB)X_2$ concentration increases from 2 μM to 30 μM (Figure 2.10). Further increasing the electrolyte concentration has no significant effect on the SERS feature for any of the $BBIB^{2+}$ halide salts, suggesting that the electrolyte reached saturation adsorption.

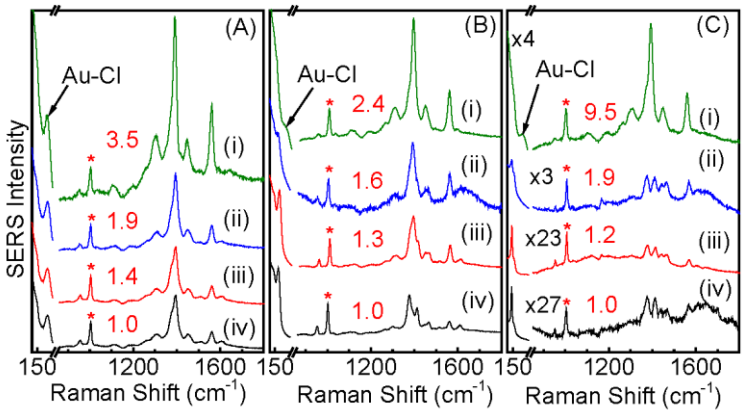

Figure 2.10 Concentration dependence of the SERS spectra of (A) $(BBIB)Cl_2$, (B) $(BBIB)Br_2$, and (C) $(BBIB)I_2$.

Note: The nominal concentrations of the electrolytes from (i)-(iv) are 2, 10, 30, and 100 μM, respectively. The nominal concentration of AuNPs is 6.5 nM. All SERS spectra were normalized to the peak at 1003.76 cm^{-1}, denoted by '*'.The spectra are normalized and offset for clarity. The normalization factors for each spectrum are shown with numbers in red. The numbers in black in spectra (ii), (iii), and (iv) in Figure 2.10(C) are the scaling factors for the spectral feature in the ~800 to 1650 cm^{-1} region in comparison to its spectral feature below 300 cm^{-1} region.

The saturation packing capacity of the as-synthesized AuNPs for $BBIB^{2+}$ in an equal volume $(BBIB)Cl_2$ and AuNP mixture is 6.3 ± 0.4 μM (Figure 2.11).

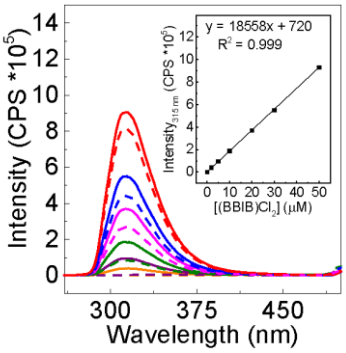

Figure 2.11 Fluorescence quantification of $BBIB^{2+}$ adsorption onto AuNPs.

Note: The spectra in solid lines were obtained with $(BBIB)Cl_2$ standard solutions prepared by using the AuNP centrifugation supernatant as the solvent. The dash lines are the emission spectra obtained with the supernatants of overnight-incubated AuNP/$(BBIB)Cl_2$. The inset is the calibration plot of the $(BBIB)Cl_2$ standards in which the nominal concentrations of $(BBIB)Cl_2$ are 0, 2, 5, 10, 20, 30, and 50 μM.

The ratio of cations and anions coadsorbed onto the AuNPs most likely changed when the electrolyte concentration changes from 2 to 30 μM. This is because the peak intensity ratio between the Au-X SERS feature and the $BBIB^{2+}$ SERS feature in 1003 cm^{-1} varies as the function of the $(BBIB)X_2$ concentration. The relative intensity of Au-Cl decreases when $(BBIB)Cl_2$ concentration increases to 30 μM, but the Au-Br and Au-I SERS intensity increases with increasing concentrations of $(BBIB)Br_2$ and $(BBIB)I_2$, respectively. Moreover, there is a relatively small, but identified Au-Cl SERS feature in SERS spectra acquired with the 2 μM $(BBIB)Br_2$ and $(BBIB)I_2$ samples. These results are most likely due to the relatively high concentration of Cl^- in the as-synthesized colloidal AuNPs in which $HAuCl_4$ was used as the gold precursor. Therefore, when $(BBIB)X_2$ concentration is low, both Cl^- and the halide in $(BBIB)X_2$ can be coadsorbed onto AuNPs with $BBIB^{2+}$. However, when $(BBIB)Br_2$ and $(BBIB)I_2$ concentration is high, no Cl^-

binding to AuNP is possible because the binding affinity of Br^- and I^- to AuNPs is higher than that for Cl^-.[29,107,108]

The concentration dependence of the amount of X^- and $BBIB^{2+}$ adsorbed can be understood on the following theoretical consideration. The coadsorption of likely-charge ions is competitive, but the coadsorption of oppositely charged ions such as $BBIB^{2+}$ and X^- onto AuNPs should be both competitive and cooperative in nature. Their competitiveness arises from the fact that both cations and anions have to compete for the limited AuNP surface available for ligand binding, while the cooperativeness stems from the electrostatic attraction between cation and anion. This competitive/cooperative nature can complicate the quantitative understanding of the effect of electrolyte concentration on ion pairing on AuNPs.

The $BBIB^{2+}$ SERS feature in the 2 μM $(BBIB)X_2$ samples are very similar for all three halides, indicating that the $BBIB^{2+}$ conformation on AuNP are similar in these samples. This result is not surprising. At this concentration, $BBIB^{2+}$ and X^- are only sparsely packed onto AuNPs in all $(BBIB)X_2$ samples. Therefore, the cross interactions among these ionic species (anion/anion, cation/anion, and cation/cation) on AuNPs themselves are likely significantly weaker. Consequently, $BBIB^{2+}$ adopts the most thermodynamically favorable conformation that maximizes its binding energy on AuNPs. However, when $(BBIB)X_2$ approaches saturation packing concentration, the electrostatic interactions among the ionic species on AuNPs become increasingly significant. These electrostatic interactions inevitably affect the most energetically favorable $BBIB^{2+}$ conformation on AuNPs.

Energetically, the Gibbs energy change associated with ligand binding to NP before the onset of NP aggregation can be written as Eq.2.1. Since the enthalpy change associated with ligand binding is likely much larger than the entropy contribution, for the simplicity of discussion, we ignore the entropy term but focus on the enthalpy variation during the ligand adsorption process.

The system's total enthalpy change associated with molecular or ionic ligand binding to AuNP can be written as Eq. 2.2 where is the enthalpy change associated with the ligand solvation states; is the binding energy of individual ligand with a neutral AuNP; and is the Coulombic potential energy change induced by the binding of ionic species to AuNPs. and should be invariably negative because they can both be classified loosely as van der Waals interactions, but can be positive or negative depending on the signs of the net charge of the NPs and incoming ligands. Furthermore, the magnitude of is highly dependent on the number of net charge and charge pairs on the nanoparticles. Since the binding of a charged species in solution onto the NP surface is unlikely to have a significant effect on the Coulombic potential energy of the solution, the value of should be totally dominated by the AuNP Coulombic potential energy change associated with ligand binding. In addition, associated with a neutral ligand can be treated as negligible.

(2.1)

(2.2)

$\Delta H = \Delta H \Delta H - T\Delta S - \Delta H_{Electrical} - \Delta H_{Solvation}$

One important implication of Eq. 2.2 is that while adsorption of a neutral ligand onto AuNPs may be approximated as Langmuir adsorption in which the binding of one molecule has no impact on the binding affinity of the incoming ligands, the adsorption of charged species onto AuNPs can be highly cooperative in nature. An electrically charged AuNP should facilitate the adsorption of ionic species with opposite charge, but reduces that for ions with the same charge.

Equations 2.1 and 2.2 facilitate conceptually specific ion effect on electrolyte-induced AuNP aggregation, even though reliable experimental determination and computational modeling of the parameters in these equations are not currently possible. The reason that MX salts differ so much from the $(BBIB)X_2$ and (AM)X in their threshold concentration (over 1000 times) in inducing AuNP aggregation is due to difference in their cation forming ion pair with halides on AuNPs. Imaginable, the $\Delta H_{L/AuNP}$ values for $(BBIB)^{2+}$ and $(AM)^{+}$ should be significantly higher than that for K^{+}. This is because $(BBIB)^{2+}$ and $(AM)^{+}$ are organic cations with extensive π electrons. The latter facilitates $(BBIB)^{2+}$ and $(AM)^{+}$ binding to AuNPs through inter-molecular van der Waals interaction. Furthermore, $\Delta H_{Solvation}$ for $(BBIB)^{2+}$ and $(AM)^{+}$ should be drastically smaller than that for K^{+}. The solubilities of the $(BBIB)X_2$ and (AM)X in water are significantly smaller (~ 10 mM) than that of MX (~ 5 M or above). When $(BBIB)^{2+}$, $(AM)^{+}$, and M^{+} are added to AuNP that contains the same amount of surface halide adsorbates, $(BBIB)^{2+}$ and $(AM)^{+}$ should be much easier to be directly attached to AuNPs than M^{+}, forming ion pair with the halides and driving the AuNP neutralization.

2.4.5 Competitive ligand adsorption onto AuNPs

Ion pairing can have significant effect on competitive ligand adsorption onto the AuNPs. Figure 2.12 shows the SERS spectra obtained with (adenine/(BBIB)X_2)/AuNP and (adenine/KI)/AuNP samples. Adenine SERS features dominate the SERS spectra in all the samples with the only exception of (adenine/(BBIB)I_2)/AuNP. Both $BBIB^{2+}$ and I^- SERS feature are present in the latter sample, but not that of adenine. The concurrent absence and appearance of $(BBIB)^{2+}$ and X^- SERS feature provides unambiguous experimental evidence for the cooperativity of electrolyte adsorption onto AuNPs.

The fact that $(BBIB)^{2+}$ and I^- SERS feature dominate the SERS spectrum of (adenine/(BBIB)I_2)/AuNP indicates that either $(BBIB)^{2+}$, I^-, or both has higher binding affinity to neutral AuNPs than adenine. However, without the ion pairing, neither $(BBIB)^{2+}$ nor I^- is effective in competing with adenine for the AuNP surfaces under the explored experimental conditions. The fact that SERS features of $(BBIB)^{2+}$ and X^- were only observed in (adenine/(BBIB)I_2)/AuNP, but not in (adenine/(BBIB)Cl_2)/AuNP or (adenine/(BBIB)Br_2)/AuNP is consistent with the I^- has higher binding affinity to AuNPs than both Br^- and Cl^-. Therefore the $(BBIB)^{2+}$ coadsorption with I^- onto AuNPs is energetically more favorable than that with Br^- or Cl^-. This makes the $(BBIB)^{2+}$ and I^- coadsorption onto AuNPs more effective than the adenine adsorption.

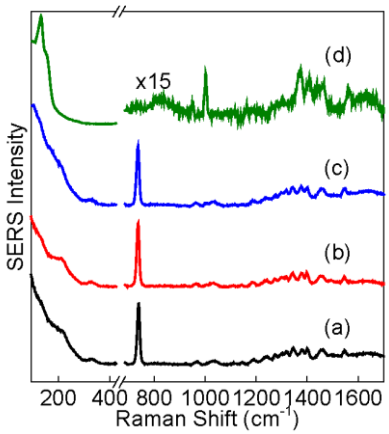

Figure 2.12 SERS spectrum of (a) AuNP/(adenine/KI), (b) AuNP/(adenine/(BBIB)Cl_2)), (c) AuNP/(adenine/(BBIB)Br_2)), and (d) AuNP/(adenine/(BBIB)I_2)).

Note: The nominal concentrations of (BBIB)X_2 or KI, adenine, and AuNPs are 20 μM in terms of halides, 10 μM, and ~6.5 nM, respectively. All spectra were scaled and offset for clarity. The number associated with spectrum (d) is the scaling factor for the spectral feature in the ~700 to 1650 cm^{-1} region in comparison to its spectral feature below 400 cm^{-1} region.

2.4.6 Solvent effect on AuNP aggregation

Ion pairing provides an alternative explanation to the solvent effect on the aggregation of the citrate-reduced AuNPs. The higher percentage of ethanol in the water/ethanol cosolvent, the less stable the AuNPs (Figure 2.13). Similar phenomenon was reported before, and it was attributed to the possible ethanol displacing capping citrate ions on AuNPs.[109] An alternative explanation to this experimental observation is that reducing the solvent polarity enhances ion pairing on AuNPs. The latter reduces the charge density on AuNPs and promotes AuNP aggregation. Indeed, nonpolar solvent enhances ion paring has long observed in solution,[82] and it is responsible for the poor electrolyte solubility in nonpolar solvent. The enhanced ion pairing on AuNP in the ethanol-containing solvent can be due to combined effects of stronger electrostatic

interaction between cation and anion in ethanol solution than that in water, and the lower solvation energy of ions in ethanol than in water. The relative permittivity (ε) of less polar solvent such as ethanol (ε ~24) is significantly lower than that for water (ε~80). These effects make the AuNPs easier to be neutralized in nonpolar solvent than in water.

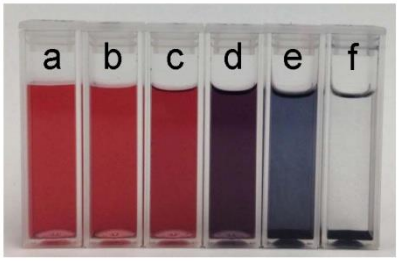

Figure 2.13 Photograph of the AuNP in the water:ethanol cosolvents where the % volume of ethanol in the cuvettes (a) to (f) varies from 0%, 13.3%, 26.7%, 40.0%, 53.3%, and 66.7% , respectively.

Note: The nominal AuNP concentration is 6.5 nM.

There are two possible scenarios could lead to the ion pairing-driven AuNP charge reduction in the (BBIB)X_2-, and (AM)X-containing AuNP solutions. First, the cations and anions were adsorbed as neutral ion pairs (salt), which partially or completely displaced the citrate ions on the as-synthesized AuNP surfaces. Such a possibility can be excluded on the fact that all the electrolyte were completely dissolved before adding to AuNPs and the strong concentration dependence of the (BBIB)X_2 SERS spectra. In fact, the threshold (BBIB)X_2 and (AM)X concentration for inducing AuNP aggregation is 2 μM, which is about 5000 times lower than their solubilities (~10 mM) in water.

The second scenario is that cations and anions are adsorbed separately onto AuNPs, but forming contact or spatially-separated ion pairs on AuNPs. The latter can be viewed as the AuNP-bridged ion pair, in analogy to the well-established solvent-

separated ion pair. While both contact and AuNP-bridged ion pairing are possible, the concentration dependence of the $(BBIB)X_2$ SERS spectra suggests the AuNP-bridged ion pairing is more prominent. Otherwise, the anion/cation ratio or the $BBIB^{2+}$ SERS feature should not have a strong dependence of the electrolyte concentration.

Attempts to use SERS to detect possible ion pairing on AuNPs between of alkali metal halide salts were unsuccessful even when AuNPs are mixed with high molar MX solution or dried together with MX. Only Au-X SERS features were observed, but no Au-M Raman feature can be identified. It is noted that the absence of Au-M stretching feature does not necessarily argue against the possibility of direct metal interaction with AuNPs or the MX ion pairing on AuNPs. Indeed, the reason of absence of the Au-M Raman feature can that the Au-M stretching frequency is too close to the laser line, or the Raman activity of Au-M stretch is too low to be observed. Indeed, it has not been possible to detect any Raman features for essentially all common metals and metal alloys. Given the extensive literature reports on the ion pairing between metal ion and halide on the air/liquid interface in concentrated metal halide solutions,[90,93,110-112] the possibility of the metal and halide ion pairing at AuNPs/liquid interface cannot be excluded.

2.5 Conclusions

Electrostatic interaction is one of the most fundamental forces in nature, and electrolyte interactions with colloidal particles have broad implication to a wide range of scientific disciplines and technological applications. We demonstrated the first definitive experimental evidence of ion pairing on liquid/solid interfaces, and its drastic effect on the electrolyte induced nanoparticle aggregations. Indeed, electrolyte can induce the nanoparticle aggregation through two pathways, both under the theoretical framework of

the EDL theory. The first is by increasing the solution ionic strength, and the second by reducing the nanoparticle surface charge density through forming ion pairs on nanoparticle surfaces. Both effects reduce the Debye-length of the EDL on nanoparticle surface and weaken the interparticle electrostatic repulsion among different nanoparticles. Evidently the first pathway can be in play for all electrolyte-induced nanoparticle aggregations because increasing electrolyte concentration increases solution ionic strength. However, for electrolytes with cations and anions that both have higher binding affinity to AuNPs than citrate, the ion paring is likely the predominant pathway for the electrolyte-induced AuNP aggregation. This is why some electrolytes such as $(BBIB)X_2$ and (AM)X shown in this work can induce AuNP aggregation even with concentration as low as low μM. The experimental results with competitive $(BBIB)X_2$, KX, and adenine adsorption onto the AuNPs confirms the cooperativity on anion and cation adsorption onto solid support. While this work provided the first direct evidence confirmation of ion pairing on AuNPs, the generality of the ion pairing in general electrolyte, especially metal halide salts, interactions remains to be investigated. Addressing this issue calls for techniques that must be not only sensitive to AuNP-metal interaction but also capable of differentiating the metal ions directly attached to AuNPs from that surrounding the AuNPs. The insights provided in this work are important for understanding electrolyte-induced AuNP aggregation and the effect of ion pairing on competitive ligand adsorption.

Notes: This work has been previously published: Perera, G.S.; Nettles II, C.B.; Zhou, Y.; Zou, S.; Hollis, T.K.; Zhang, D., Direct Observation of Ion Pairing at the Liquid/Solid Interfaces by Surface Enhanced Raman Spectroscopy. *Langmuir* **2015**, *31*, 8998-9005.

CHAPTER III

COUNTERION EFFECTS ON ELECTROLYTE INTERACTIONS WITH GOLD NANOPARTICLES

(Published in *J. Phys. Chem. C* **2016**, *120*, 23604-23612)

3.1 Abstract

Electrolyte interactions with nanoparticles (NPs) at solid/liquid interfaces are highly complicated as the charged species can be directly adsorbed onto the NP surfaces, confined in the diffusion layer immediately surrounding the NPs, and dispersed in bulk solution. Existing studies on electrolyte interactions with NPs are based primarily on the electrical double layer theory that focuses mainly on electrolyte interactions with NPs with fixed pre-existing charges. Demonstrated herein is a comprehensive study of counterion effects during the electrolyte bindings to gold nanoparticles (AuNPs), including halide-induced AuNP aggregation and fusion, quantitative cation and anion coadsorption, selective cation and anion displacement on AuNPs, and surface enhanced Raman spectroscopic features of the ionic species adsorbed onto AuNP surfaces. In contradiction to previous reports that electrolyte effects are anion-specific, we demonstrated that cations can play a dominant role in the halide-induced AuNP aggregation and fusion and the ion exchange processes on AuNP surfaces. Mechanistically, these counterion effects are due to the cooperative and competitive cation and anion binding to AuNPs and AuNP-facilitated cation and anion interactions.

3.2 Introduction

Electrolyte interactions with colloidal nanoparticles (NPs) in aqueous solutions have been implicated in a wide range of researches and applications.[11,12,44,113] One of the most important observations is that electrolytes of high concentrations can induce NP aggregation.[20,29,114] This phenomenon can be readily understood by the electrical double layer (EDL) theory.[115-117] However, the existing EDL model accounts only for electrolyte interactions at the solid/liquid interfaces with fixed pre-existing charges and how such interactions may alter electrolyte concentrations.[78,117,118] It provides very limited information on how electrolytes directly bind to NPs and their impact on the charge density and distribution of NP, and NP morphological modifications. Furthermore, the countable studies on electrolyte binding to NPs focused primarily on either cations or anions,[21,22,24,25,29] while the potential cation and anion coadsorption onto NPs and NP-facilitated cation−anion interactions remain largely uncharted. Filling this knowledge gap is critical to develop the mechanism of electrolyte binding to NPs.

Unlike the binding of neutral molecules in which the entire molecules are adsorbed as one identity, interactions of ionized electrolytes with the solid surface are drastically more complicated, and several different scenarios could occur therein. First, only cations or anions are directly adsorbed on NP surfaces and their oppositely-charged counterions are located in the diffusion layer, an analogy to solvent-separated ion pairing that is often invoked in the ion-exchange chromatography.[82,83,93] In this case the net charge on NP surfaces depends on the number and charge states of adsorbed cations or anions. The second is that cations and anions initially dispersed in aqueous solution are both adsorbed and colocalized onto NPs and form compact ion pairs, which can be

viewed as NP-assisted ion pairing and the binding of an electrolyte is equivalent to that of a neutral ligand. The third is that both cations and anions are directly adsorbed onto NPs but at different spatial locations. In this case, the electrolyte forms surface-separated ion pairs, and the net charge of NPs can be zero, positive, or negative depending on the relative number of adsorbed anions vs. cations and the charge state of ions.

Experimental characterizations of cations and anions at the solid/liquid interfaces represent a challenging analytical task. First, the analytical technique should have sufficient sensitivity to detect the miniscule amount of cations and anions at the solid/liquid interfaces. Second, this technique should be capable of differentiating the ionic species that are directly adsorbed onto the solid surface, dispersed in the bulk phase, and confined in the diffusion layer that is within a few nanometers from the solid surface. Recently, we have demonstrated that surface enhanced Raman spectroscopy (SERS) in combination with KNO_3 washing is highly effective for probing cations and anions directly adsorbed onto the AuNP surfaces.[119] SERS is a strictly near-field technique and detects only cations and anions that are either directly adsorbed onto, or located in a close vicinity (<5 nm) to, AuNP surfaces.[61,63,120,121] The electrolyte washing step enables the differentiation of electrolytes directly adsorbed onto AuNPs from those in the diffusion layer, because the washing electrolyte, KNO_3, has very low binding affinity to AuNPs and hence only displaces the ionic species in the diffusion layer surrounding the charged AuNPs. This strategy has enabled the direct observation of ion pair formation for a series of halide salts on AuNPs.[119] Noting that unlike ion pairing in aqueous solutions where the oppositely charged ions are either in direct contact or separated by a solvation shell, the

ion pairing on AuNPs refers to cation and anion coadsorption onto the same NP surfaces regardless of the separation distance.

Presented herein is a comprehensive study of counterion effects observed during the binding of electrolytes onto AuNPs, including the halide-induced AuNP aggregation and fusion, quantitative cation and anion adsorption, selective cation and anion displacement, and SERS spectra of the ionic species adsorbed onto AuNPs. The model electrolytes include 1,3-bis(3′-butylimidazolium)benzene dihalide salts ((BBIB)X_2, where X= Cl^-, Br^-, I^-), 1-allyl-3-methylimidazolium halide salts ((AM)X, where X= Cl^-, Br^-, I^-) (Figure 3.1), and a series of inorganic salts including alkali metal electrolytes (AME) such as KX (X= Cl^-, Br^-, I^-), Na_2S, and $AgNO_3$. Several of these model electrolytes were used in our previous work of ion pairing on AuNPs.[119] While there are extensive reports on electrolyte binding on colloidal AuNPs, most of them focus on the AuNP dispersion stability and effect of anions. To our knowledge, the counterion effects especially the effects of cations on the electrolyte-induced AuNP fusion, quantitative cation and anion adsorption, ion exchange, and SERS spectroscopy have not been reported. Indeed, it has been proposed that the electrolyte effects on dispersed NPs are anion-specific.[78,122] However, a more in-depth research is required to examine the validity of this highly generalized statement considering the diversity of cations. As will be shown in this work, both cations and anions affect the halide-induced AuNP aggregation and fusion, and the effect of cations rather than anions is obviously more drastic. After demonstrating these counterion effects successively, their mechanisms were elaborated that allowed to reconsider and broaden the application of the current EDL theory.

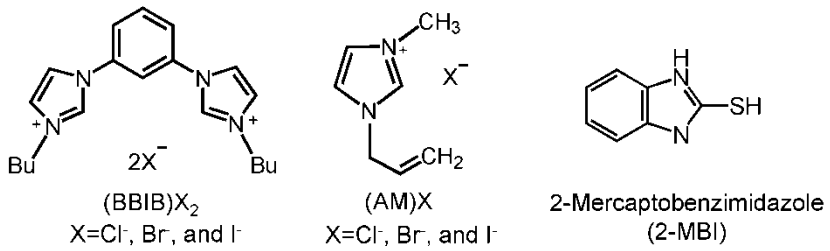

Figure 3.1 Molecular structures of the model electrolytes used in this study.

3.3 Experimental section

3.3.1 Materials and equipment

$(BBIB)X_2$ salts were prepared following the procedure given elsewhere,[98] and all other chemicals were purchased from Sigma-Aldrich. SERS spectra were acquired using the LabRam HR800 confocal Raman microscope system with a 633 nm HeNe Raman excitation laser. Inductively coupled plasma-mass spectroscopy (ICP-MS) analysis of Br^- and I^- adsorption was conducted with PerkinElmer ELAN DRC II ICP-MS instrument.

3.3.2 AuNP synthesis

AuNPs were synthesized using the same citrate reduction method as described in the experimental section in chapter two.

3.3.3 Electrolyte-induced AuNP aggregation

Equal volumes of AuNPs and KX, (AM)X, and $(BBIB)X_2$ in water with pre-defined concentrations were vortex mixed. The solutions were incubated overnight before scanning electron microscopy (SEM), photography, and 2-mercaptobenzimidazole (2-MBI) adsorption characterization of the electrolyte-induced AuNP aggregation, and fusion.

3.3.4 SEM images

The SEM images of the aggregated AuNPs were taken using a JEOL 6500F scanning electronic microscope. The AuNP aggregates were washed extensively with 18 MΩ-cm Nanopure water before depositing on a silicon wafer. A thin gold layer (~3 nm) was sputter coated onto the aggregated AuNPs before SEM acquisition. The accelerating voltage for the SEM measurement is 5 kV.

3.3.5 Quantitative 2-MBI adsorption onto electrolyte-induced AuNP aggregates

Equal volumes of AuNPs and electrolytes with pre-defined concentrations were mixed and stored overnight to allow for AuNP aggregation and precipitation. The settled AuNP aggregates were washed extensively with 18 MΩ-cm Nanopure water to remove excess electrolytes. A known amount of 50 μM 2-MBI was then added to the AuNP aggregates and 2-MBI adsorption onto AuNPs was monitored by UV-vis quantification to determine the amount of 2-MBI remaining in the supernatant of the 2-MBI/AuNP mixture solutions. The amount of adsorbed 2-MBI was determined after the concentration of 2-MBI in the supernatant remains unchanged. The concentration of 2-MBI in solution was calculated on basis of its molar absorptivity of 27,400 cm^{-1} at 300 nm.[123] The surface area of the aggregated AuNPs was estimated based on the packing density of 2-MBI on AuNPs, which equals 570 $pmol/cm^2$.[123,124]

3.3.6 Normal Raman and SERS acquisition

The normal Raman spectra of $(BBIB)X_2$ were acquired with filtered saturated solutions using a syringe filter with 100 nm pore membrane. The spectra were acquired with a 10× objective and laser power of 1.3 mW before objective. The SERS spectra

were acquired by transferring the 20 μL sample solutions that contained AuNP aggregates on stainless steel substrates. All AuNP aggregates were kept wet during the SERS acquisition process to avoid thermal damage caused by AuNP photon absorption. The spectral integration time varied from 20 to 100 s with 1 to 10 accumulations.

3.3.7 ICP-MS quantification of Br^- and I^- adsorbed onto AuNP aggregates

The Br^- and I^- adsorption were quantified through two independent ICP-MS measurements. The first is ICP-MS quantification of the difference between halides added into AuNP and halides remaining in the supernatant in the AuNP/electrolyte mixtures. The second method proceeds by first splitting the AuNP/electrolyte solution into two equal volume portions, and only the bottom portion contains the AuNP aggregates. Bromide and iodide adsorbed onto AuNPs were analyzed after adding equal amounts of aqua-regia into the top and bottom portions to completely digest the aggregated AuNPs. A bench-top centrifugation machine was used to separate AuNPs from the excess electrolytes for AuNP/electrolyte samples where electrolyte concentration is too low to induce AuNP aggregation and precipitation.

3.3.8 Fluorescence quantification of $BBIB^{2+}$ adsorption

Fluorescence measurements were conducted with a Horiba JobinYvon FluoroMax-4 spectrofluorometer in 1 × 1 cm cuvettes. The excitation wavelength was set to 252 nm and $(BBIB)^{2+}$ showed a maximum emission at 315 nm. An equal volume of AuNP supernatants was mixed with $(BBIB)X_2$ of pre-defined concentrations and reacted overnight. The fluorescence signals of the supernatants resulted from $BBIB^{2+}$ remaining free in solution. A calibration plot of $BBIB^{2+}$ fluorescence intensity at 315 nm as a

function of $(BBIB)X_2$ concentration was acquired using $(BBIB)X_2$ concentrations of 2, 5, 10, 20, 30, and 50 μM dissolved in AuNP supernatants obtained by centrifugation of the as-synthesized AuNPs. We used the AuNP supernatant, instead of water, as the solvent in the preparation of the calibration plot of $BBIB^{2+}$ is to ensure the ionic strength and composition in the $BBIB^{2+}$ calibration and measurement samples are the approximately the same. This estimation is made by assuming proton, gold, and citrate ions are completely consumed during the AuNP synthesis and only Na^+ and Cl^- in the as-synthesized colloidal AuNP solutions.

3.3.9 X-ray photoelectron spectroscopy (XPS) analysis

After washing thoroughly with 18 MΩ-cm Nanopure water, the electrolyte-treated AuNP aggregates were deposited on silicon wafers that were washed with 18 MΩ-cm Nanopure water and dried with N_2 gas before XPS measurements. XPS analysis was performed by using a Thermo Scientific K-Alpha XPS system equipped with a monochromatic X-ray source at 1486.6 eV corresponding to the Al Kα line. The spot size was 400 μm^2 and the takeoff angle of the collected photoelectrons was 90˚ relative to the sample surface. The base pressure of the instrument was at 1.0×10^{-9} mBar. The pass energy for acquisition of the survey spectra was 200 eV and the pass energy for the high resolution core level spectra was 40 eV. An average of 20 scans was performed for each sample, with a step size of 0.1 eV. All the measurements were performed in the Constant Analyzer Energy mode. “Avantage v5.932” software was used in XPS data analyzing. The XPS measurements were performed by Dr. Felio Perez in University of Memphis.

3.3.10 Zeta potential measurements of AuNPs/KX and AuNP/(BBIB)X_2

Equal volumes of pre-defined concentrations of KCl, KI, (BBIB)Cl_2, and (BBIB)I_2 were mixed with AuNPs, vortex mixed, and allowed to for five hours before acquiring the zeta potential measurements. ZetaPALS analyzer (Brookhaven Instruments Corporation (BIC), Holtsville, NY) was used to collect the zeta potential measurements at 25 ˚C. Phase Angle Light Scattering and Electrophoresis Light Scattering measurements were detected at 90˚ and 15˚ angles, respectively. The measurements were performed after the sample was stabilized in the cuvette for 3 min and total of 10 measurements were acquired for each sample.

3.4 Results and discussion

3.4.1 Counterion effect on AuNP aggregation

The counterion effects on AuNP dispersion stability in water are demonstrated by investigating the electrolyte-induced AuNP aggregation. It is noted that although there is extensive literature on the electrolyte effect on the AuNP dispersion stability in water; most of them focus on anions, and it is believed that the ability for anions for stabilizing ligand-free AuNPs follows the well-known Hofmeister series.[78,122,125]

However, Figure 3.2 clearly indicates that both anions and cations have significant effects on the AuNP dispersion stability in water. The plots in the same row are for electrolytes with the same cation but different anions (X= Cl^-, Br^-, I^-), while the plots of the same column have the same anions but different cations. Evidently, the threshold concentrations for inducing AuNP aggregation differ significantly for these halide salts; e.g., $BBIB^{2+}$ and $(AM)^+$ halide salts for inducing the complete AuNP aggregation and precipitation require not more than 5 μM, whereas the K^+ halide salts are

~20 mM, 4000 times higher than those of $(BBIB)^{2+}$ and $(AM)^{+}$ halide salts. Because the only difference among these electrolytes is cations, the apparent difference in their threshold concentrations for inducing AuNP aggregation explicitly manifests the drastic cation effects on the AuNP aggregation.

In contrast, the change of anions (X= Cl^-, Br^-, I^-) results in much smaller difference. This is in sharp contrast to the previous report that the electrolytes on AuNP dispersion stability are anion-specific.[122] In addition, Figure 3.2 explicitly shows the cations rather than anions have played a dominant role during the electrolyte-induced AuNP aggregation processes.

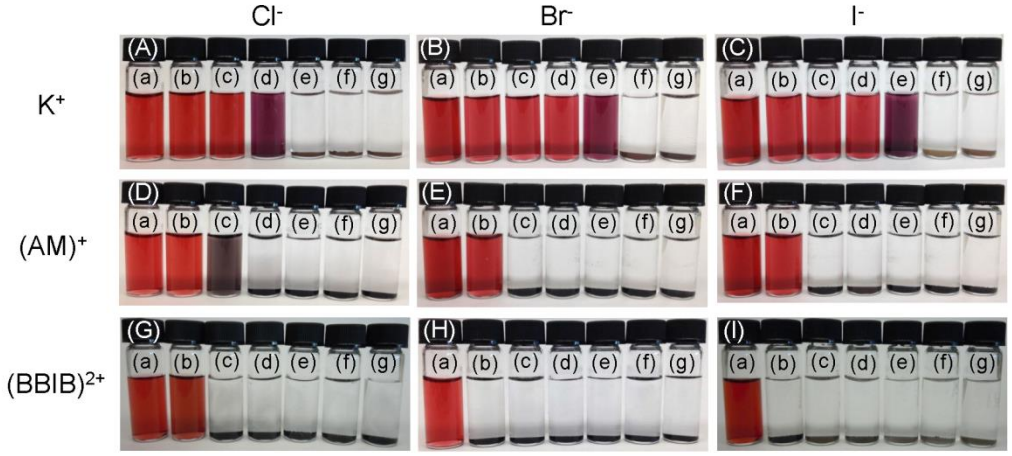

Figure 3.2 Ion-specific effects on the electrolyte-induced AuNP aggregation. The electrolytes are (A) KCl, (B) KBr, (C) KI, (D) (AM)Cl, (E) (AM)Br, (F) (AM)I, (G) $(BBIB)Cl_2$, (H) $(BBIB)Br_2$, and (I) $(BBIB)I_2$.

Note: The nominal concentration of AuNPs is 6.5 nM. For K^+-containing electrolytes (A-C), the electrolyte concentrations from (a) to (g) 0, 2, 5, 10, 20, 30, and 50 mM, respectively. For $(AM)^+$- and $(BBIB)^{2+}$-containing electrolytes (D-I), the concentrations from (a) to (g) are 0, 2, 5, 10, 20, 30, and 50 μM, respectively. The photographs are taken after overnight incubation.

3.4.2 Counterion effect on the halide-induced AuNP fusion

Halide ions (Cl^-, Br^-, and I^-) are known for the ability to induce AuNP fusion.[21,23,29] However, the effect of counterions in halide electrolytes on the AuNP fusion has to our knowledge not been explored. The difference in AuNP fusion induced by the various halides can be readily seen from the SEM images and photographs, as well as the measured surface areas using 2-MBI as probe molecule (Figure 3.3).[123,124] The AuNPs aggregated by (AM)X and (BBIB)X_2 salts are black, but those aggregated by KX are orange because of the high degree of AuNP fusion (X= Cl^-, Br^-). The grain sizes of AuNP aggregates in KBr and KCl salts are significantly larger than in their respective $(AM)^+$ and $(BBIB)^{2+}$ salts. Moreover, the grain sizes of AuNPs aggregated in iodide salts are all significantly larger than those in Cl^- and Br^- salts with the same cations. This is consistent with the previous results that I^- is more effective than Br^- and Cl^- for inducing AuNP fusion.[21,23,29] However, the large differences in the surface areas of AuNPs aggregated by the K^+, $(AM)^+$, and $(BBIB)^{2+}$ salts with the same anions provides the first experimental evidence that cations can also have pronounced effects on the halide-induced AuNP fusion. Indeed, for a given halide ion, the specific surface areas of AuNPs corresponding to different cations always increase in the order of $K^+ < (AM)^+ < (BBIB)^{2+}$ (Figure 3.3(J)).

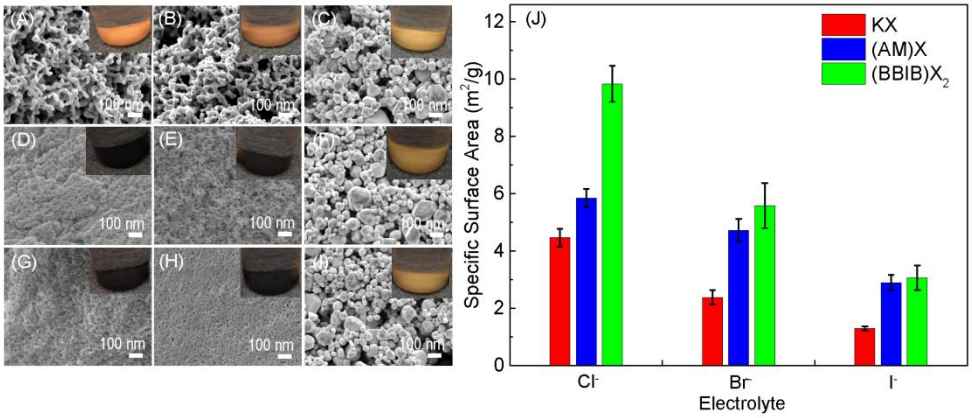

Figure 3.3 (Left) SEM images and photographs (insets) of AuNP aggregates formed in AuNP/electrolyte mixtures. The electrolytes are (A) KCl, (B) KBr, (C) KI, (D) (AM)Cl, (E) (AM)Br, (F) (AM)I, (G) (BBIB)Cl_2, (H) (BBIB)Br_2, and (I) (BBIB)I_2. (Right) Comparison of the specific surface areas of AuNP aggregates using quantitative 2-MBI adsorption.

Note: The nominal concentrations of AuNPs and electrolytes are 6.5 nM, and 50 mM, respectively. The photographs are taken after overnight incubation of AuNP/electrolyte solutions. SEM images are acquired after extensively washing the overnight incubated AuNP aggregates.

3.4.3 Counterion effects on electrolyte adsorption

The counterion effects on electrolyte interactions with AuNPs are also manifested in the quantitative electrolyte adsorption to AuNPs. Figure 3.4(A) compares $(BBIB)^{2+}$ adsorption onto AuNPs in the AuNP/(BBIB)X_2 mixtures, while Figures 3.4(B) and 3.4(C) compare Br^- and I^- adsorption onto AuNPs mixed with KX, (AM)X, and (BBIB)X_2 (X=Br^-, I^-), respectively. The quantification of $(BBIB)^{2+}$ adsorption is performed using the fluorescence spectroscopy, while those of Br^- and I^- adsorption are evaluated using ICP-MS. In principle, the ions quantified in Figure 3.4 should include ions directly adsorbed onto the AuNP surfaces and the excess ion confined in the diffusion layer surrounding the AuNPs. Nonetheless, the contribution of detected ions in the diffusion layer should be vanishingly small, because of the highest concentration of

ions added into AuNP solutions is 50.0 μM for Br^- and I^-, while the baseline Cl^- and Na^+ in the as-synthesized AuNP solutions are 4.0 and 10.5 mM, respectively. Accordingly, the excess cations and anions to be confined at the diffusion layer surrounding the charged AuNPs are likely to be the much more concentrated Na^+ or Cl^- instead of the added low-concentration $(BBIB)^{2+}$, Br^-, or I^- in solutions.

The quantification of Cl^- adsorption is difficult because of its poor ICP-MS sensitivity. The maximal amounts of $(BBIB)^{2+}$ absorbed onto AuNP surfaces are different in the various halide salts and decrease in the order $(BBIB)Cl_2$ (6.3±0.4 μM) > $(BBIB)Br_2$ (5.2±0.5 μM) > $(BBIB)I_2$ (3.9±0.4 μM), in spite of the fact that the amounts of AuNPs used in these studies are equivalent. This clearly indicates that the amount of $(BBIB)^{2+}$ adsorbed onto AuNPs depends critically on the choice of anions.

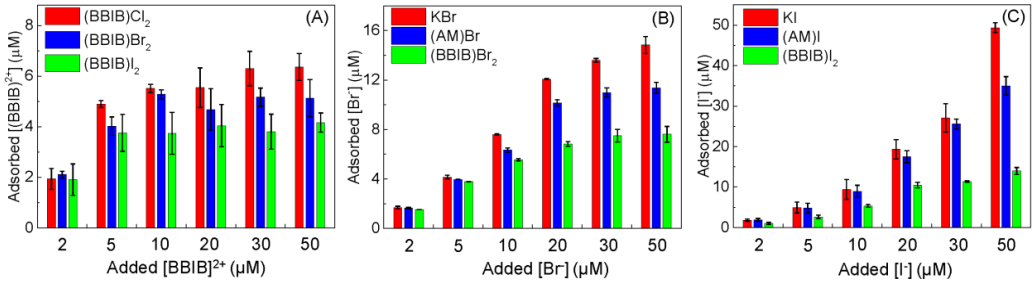

Figure 3.4 (A) Comparison of concentration-dependent $BBIB^{2+}$ adsorption onto AuNPs in AuNP/$(BBIB)X_2$. (B) and (C) Comparison of X^- adsorption onto AuNPs in AuNP mixed with KX, (AM)X, and $(BBIB)X_2$, with X standing for Br^- in (B), and I^- in (C), respectively.

Note: The calibration curve of the $BBIB^{2+}$ quantification is shown in Figure 2.11 in chapter two. It is noted that the vertical scale in these plots are significantly different.

In a similar way, cations have significant effect on the anion adsorption onto AuNPs. The amounts of adsorbed halides decrease drastically when the counterions

change from K^+ to $(AM)^+$ and then to $(BBIB)^{2+}$. Surprisingly, the quantities of I^- and Br^- adsorption onto AuNPs in both K^+- and $(AM)^+$-containing samples increase monotonically with electrolyte concentrations (Figure 3.4B and 3.4C), while they can both reach an approximately constant adsorption in their corresponding $(BBIB)^{2+}$-containing samples. Detail reason for this experimental observation is unclear. Nonetheless, the drastic differences in Br^- and I^- adsorption on AuNPs among their respective K^+, $(AM)^+$, and $(BBIB)^{2+}$ salts demonstrate that the anion binding affinities and adsorption capacities on AuNPs depending critical on the cations presented in the solutions.

3.4.4 Counterion effects on the SERS spectrum of ions on AuNPs

For the sake of simplicity, the notation of (A/B)/C was used to represent the solution mixture prepared by mixing the two components (A and B) before adding component C. Figure 3.5 shows the SERS spectra obtained with $(BBIB)X_2$ alone and mixed with AME, KCl, KBr, KI, and Na_2S, respectively. Besides the indicated anion features, all other spectral features in these SERS spectra should be aroused by $(BBIB)^{2+}$.[101-105,119,126,127] This is because alkali metals are Raman inactive and each halide has only one SERS peak corresponding to Au-X stretching. Sulfide (S^{2-}) has two SERS peaks that are caused by the Au-S stretching at ~260 cm^{-1} [126,127] and polysulfide stretching at ~450 cm^{-1}.[126] Evidently, the $(BBIB)^{2+}$ SERS spectral features including the peak intensities and correlations depend critically on the identity of anions present in the $(BBIB)^{2+}$/AuNP mixture solutions. For example, the SERS features of $BBIB^{2+}$ paired with I^- are significantly different from those paired with S^{2-}, Br^-, and Cl^- (Figure 3.5).

The counterion effects on the SERS spectra for ionic species adsorbed onto AuNPs have, to our knowledge, not been reported before. The likely reason of the counterion effects observed in the $(BBIB)^{2+}$ SERS spectra is the AuNP-facilitated cation and anion interactions, while the exact mechanism of such cross-interactions currently remains unclear. However, as a conductive nanomaterial, AuNP should be able to facilitate the charge transfers between surface-adsorbed cations and anions, as will be further discussed later.

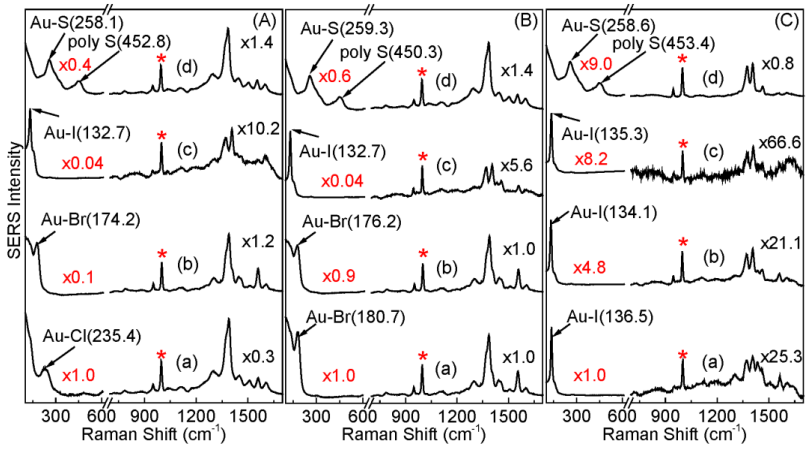

Figure 3.5 SERS spectrum of (A) (AuNP/$(BBIB)Cl_2$))/AME, (B) (AuNP/$(BBIB)Br_2$))/AME, and (C) (AuNP/$(BBIB)I_2$))/AME.

Note: Spectra (a) in the plots are AuNP/$(BBIB)X_2$ control.The AME for spectra (b) and (c) are KBr and KI, respectively in Figures 3.5A; KCl and KI, respectively in Figure 3.5B; and KCl and KBr, respectively, in Figure 3.5C. The AME for spectrum (d) is Na_2S. The nominal concentrations of AuNPs, $(BBIB)X_2$, and AME are 10 nM, 25 µM, and 1 mM, respectively. All the SERS spectra were normalized to the peak at 1003 cm^{-1} denoted by '*'. The number in red is the between-spectrum normalization factors. The numbers in black are the within-spectrum scaling factors for normalizing the spectral features in the ~700-1700 cm^{-1} region to that below ~625 cm^{-1} region in the same spectrum. The within-spectrum scaling was performed before spectrum normalization.

3.4.5 Counterion effect on the ion exchange on AuNPs

The counterion effects on electrolyte binding to AuNPs are also reflected in Ag^+ displacing $(BBIB)^{2+}$ where Ag^+ and $(BBIB)^{2+}$ are coadsorbed with halides and S^{2-} onto AuNP surfaces. Among all nitrates explored in this work that include KNO_3, $Mg(NO_3)_2$ and $AgNO_3$, only $AgNO_3$ can induce the significant displacement of $(BBIB)^{2+}$ from AuNP surfaces in the AuNP/$(BBIB)X_2$ and AuNP/$((BBIB)Cl_2/Na_2S)$ samples (Figure 3.6). Such ion-induced ligand displacement has not been reported before. More importantly, the threshold $AgNO_3$ concentration that induces the complete disappearance of $(BBIB)^{2+}$ SERS signal in the $AgNO_3$-treated AuNP/$(BBIB)X_2$ and AuNP/$((BBIB)Cl_2/Na_2S)$ depends critically on the choice of anions that are coadsorbed with $BBIB^{2+}$ on AuNPs. $AgNO_3$ with the concentration as low as 100 μM causes the complete disappearance of the SERS feature of $(BBIB)^{2+}$ that is initially paired with S^{2-} on the AuNP surface in the AuNP/$((BBIB)Cl_2/Na_2S)$ sample (Figure 3.6D). In contrast, there is a residual $(BBIB)^{2+}$ SERS feature in the $AgNO_3$-treated AuNP/$(BBIB)X_2$ even when the $AgNO_3$ concentration is raised to as high as 1.0 M.

The mechanisms of the anion exchange shown in Figure 3.5 and the $(BBIB)^{2+}$ removal shown in Figure 3.6 are likely fundamentally different. For the anion exchange observed in the (AuNP/$(BBIB)X_2$))/AME samples, anions in AME should have a higher binding affinity to AuNP in the initial anion X^- coadsorbed with $(BBIB)^{2+}$ on the AuNP in order to produce the significant anion exchange. In other words, the anion exchange proceeds through ligand displacement on AuNP surfaces and it reflects the competitive nature of the AuNP binding of the ions with the same charge sign. However, the Ag^+-induced $(BBIB)^{2+}$ removal from AuNP surfaces is assumed to proceed through charge

neutralization in which anions initially paired with $(BBIB)^{2+}$ on AuNPs react with Ag^{+} and form insoluble charge-neutral AgX or Ag_2S on AuNP surfaces. The neutralization of these anions increases the electrostatic repulsion among $(BBIB)^{2+}$ cations, thus destabilizing them on AuNP surfaces. As a result, the initial $(BBIB)^{2+}$ and X^{-} ion pairs on AuNPs can be replaced by the insoluble charge-neutral AgX or Ag_2S.

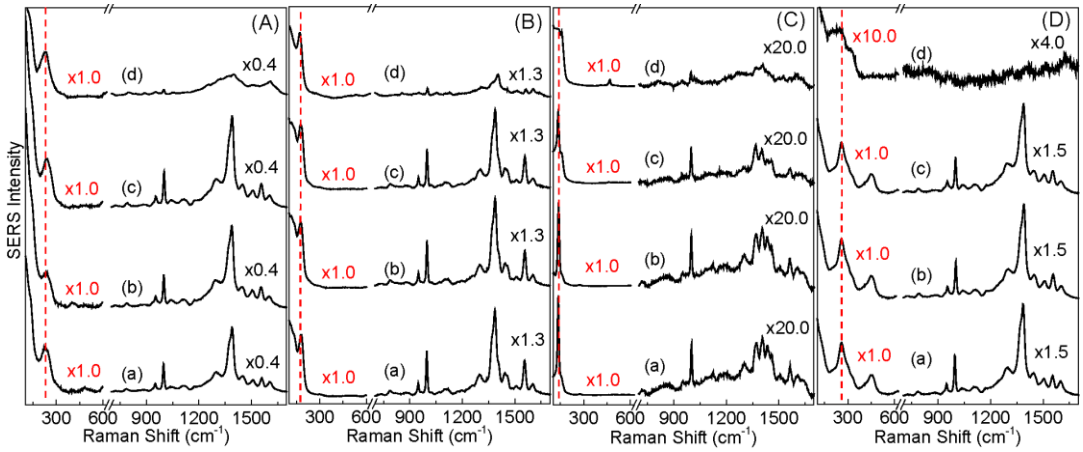

Figure 3.6 SERS detection of $BBIB^{2+}$ displacement by K^{+}, Mg^{2+}, and Ag^{+} in (A) AuNP/$(BBIB)Cl_2$, (B) AuNP/$(BBIB)Br_2$, (C) AuNP/$(BBIB)I_2$), and (D) AuNP/$((BBIBCl_2)/Na_2S)$.

Note: Spectrum (a) in (A-C) is AuNP/$(BBIB)X_2$ control, and (a) in (D) is AuNP/$((BBIB)Cl_2/Na_2S)$. Spectra (b), (c), and (d) are acquired after overnight incubation of sample (a) with KNO_3, $Mg(NO_3)_2$, and $AgNO_3$, respectively. The KNO_3 and $Mg(NO_3)_2$ concentration are both 1 M. The $AgNO_3$ concentration in (A), (B), (C), and (D) are 1 M, 1 M, 1 M, and 100 µM, respectively. The nominal AuNPs and $(BBIB)X_2$ concentrations are 10 nM and 50 µM, respectively. The numbers in red are the scaling factors between the spectra shown in the same plot. The numbers in black are the scaling factors for normalizing the features in the ~700-1700 cm^{-1} region to the spectral features below ~625 cm^{-1} region in the same spectrum. The within-spectrum scaling was performed before between-spectrum normalization. The red dash line corresponds to the position of Au-X stretching feature in (A), (B), and (C), and Au-S in (D).

The charge-neutralization hypothesis is consistent with the data of solubility products that decline as AgCl (2×10^{-10} M^2)[128,129] > AgBr (5×10^{-13} M^2)[130,131] > AgI (8×10^{-17} M^2)[125,132] > Ag_2S(6×10^{-51} M^3).[133,134] The solubility products clearly indicate that Ag^+ is easier to form charge- neutral molecules with S^{2-} as compared to I^-, Br^- and Cl^-.

The formation of AgX on $AgNO_3$-treated (AuNP/(BBIB)X_2) is further verified by XPS analyses of the (AuNP/(BBIB)I_2)/$AgNO_3$ sample which shows an appreciable amount of I^- and Ag^+ coadsorbed onto AuNP surfaces (Figure 3.7).

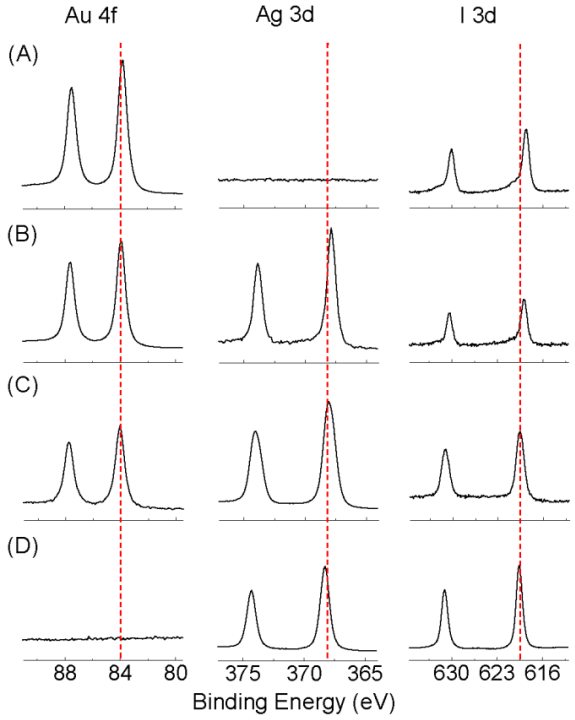

Figure 3.7 XPS spectra of washed precipitates of (A) AuNP/(BBIB)I_2, (B) (AuNP/(BBIB)I_2)/$AgNO_3$, (C) ($AgNO_3$/(BBIB)I_2)/AuNP, and (D) $AgNO_3$/KI.

Note: Spectra from left to right represent XPS spectra for Au 4f, Ag 3d, and I 3d, respectively. The nominal concentrations of AuNPs, (BBIB)I_2, $AgNO_3$, and KI are 6.5 nM, 100 µM, 1 M, and 1 M, respectively. Spectra were normalized to the spectral acqusition time. Vertical red lines are for guiding views.

3.4.6 Origin of counterion effects on the electrolyte binding to AuNPs

Mechanistically, the experimentally observed counterion effects presented above cannot be explained by the current EDL theory alone that mainly focuses on how electrolytes affect the electrostatic interactions of charged NPs and the local electrolyte concentrations surrounding the charged NPs. It takes ion pairing in combination with the EDL theory to offer a reasonable interpretation to the observed counterion effects. Taking the electrolyte effects on NP aggregation as an example, the electrolyte-induced AuNP aggregation can proceed through two possible pathways. The first is charge-screening that is likely to be responsible for KX-induced AuNP aggregation wherein the electrolyte concentrations have to be sufficiently high in order to reduce the electrostatic repulsions among the charged AuNPs and result in their aggregation. This is the commonly invoked pathway in literatures for interpreting the electrolyte-induced AuNP aggregation.[20,29,114]

The second is the charge neutralization pathway in which the dispersed cations and anions are coadsorbed onto AuNPs, and the charge densities on AuNP surfaces and electrostatic repulsion among AuNPs are thus diminished, leading to AuNP aggregation. The (AM)X- and (BBIB)X_2-induced AuNP aggregation should proceed through the second pathway. This is because the threshold concentrations for these electrolytes to induce AuNP aggregation are apparently too low to produce the substantial charge-screening effect. This charge-neutralization hypothesis is also supported by the zeta-potential measurements (Figure 3.8). The threshold concentrations to drastically reduce the AuNP zeta potentials (by 50%) are below 1.5 μM for (BBIB)X_2 while above 10.0 mM for KX.

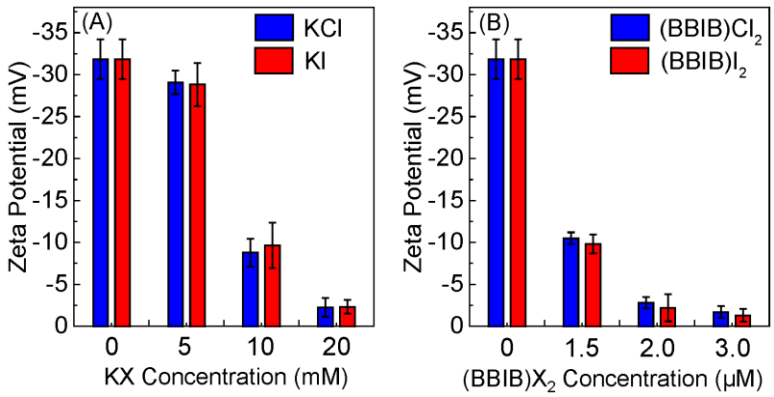

Figure 3.8 Zeta potentials for the AuNPs mixed with different concentrations of (A) KX and (B) $(BBIB)X_2$.

Note: The nominal concentration of AuNPs was ~6.5 nM. The measurements were conducted ~10 mins after mixing the electrolyte with AuNPs.

The counterion effect can be highly NP-specific. Therefore the conclusions drawn from one type of NPs might not necessarily applicable to other types. As an example, when using polystyrene NPs (PSNPs) instead of AuNPs as the model, there is no notable difference among these electrolytes in their induction of PSNP aggregation. The PSNP beads remain stable in all electrolyte solutions even when these electrolyte concentrations are raised to as high as 10.0 mM. This is in sharp contrast to the AuNPs treated by the same series of halide salts where $(BBIB)^{2+}$ and $(AM)^{+}$ halide salts of μM level can induce the significant AuNP aggregation.

The drastic cation dependence among the $(BBIB)^{2+}$, $(AM)^{+}$, and K^{+} halide salts in their ability to induce AuNP aggregation and reduce halide-induced AuNP fusion is likely due to the fact that as organic cations, $(BBIB)^{2+}$ and $(AM)^{+}$ possess π and n electrons and show higher binding affinities to AuNPs than alkali metal K^{+}. In addition, $(BBIB)^{2+}$ and $(AM)^{+}$ should have smaller hydration energies than K^{+}. These two effects

cause $(BBIB)^{2+}$ and $(AM)^{+}$ rather than K^{+} to be more facilely coadsorbed with halide ions onto AuNPs and more effectively reduce the charge densities on AuNP surfaces, as supported by the cooperative cation and anion binding to AuNP surfaces observed in a series of competitive ligand binding experiments.[119] In the earlier study, it is demonstrated that $(BBIB)^{2+}$ and I-Au SERS features appear only in the (AuNP/(adenine/$(BBIB)I_2$)) sample, but no $(BBIB)^{2+}$ SERS or I-Au SERS feature can be seen respectively in (AuNP/(adenine/$(BBIB)Cl_2$)) or (AuNP/(adenine/KI)). The SERS spectra of the latter two samples are totally dominated by adenine SERS feature.[119] The results clearly state that the cooperative $(BBIB)^{2+}$ and I^- binding to AuNPs is necessitated in order for these two ions to have adequate binding affinity to compete with adenine for the AuNP surface. Otherwise, neither I^- nor $(BBIB)^{2+}$ has sufficient binding affinity to compete with adenine for AuNPs.[119]

Besides their cooperativity, the direct cation and anion binding to AuNPs can also be competitive when the AuNP surface area is limited in comparison to the amount of added electrolytes. The data obtained with samples where the electrolyte concentrations are higher than 10 μM (Figure 3.4) indicate that the stronger the cation binding to AuNPs, the less amount of anion is adsorbed onto AuNPs, and vice versa. The competition between direct cation and anion adsorption occurs when the AuNP surface area is too small to accommodate all the ionic species in the ligand binding solutions.

3.5 Conclusions

Electrolyte interactions with NPs are highly complicated phenomena. The data presented in this work indicate that the binding, structure and properties of an ionic species on AuNPs can depend significantly on counterions present in the ligand binding

solutions. These counterion effects include electrolyte-induced AuNP aggregation and fusion, quantitative cation and anion adsorption onto AuNPs, selective cation and anion displacement on AuNPs, and the SERS spectral feature of the ionic species on AuNP surfaces. The data presented in this work highlight the critical importance to consider the potential cooperative and competitive cation and anion adsorption when studying electrolyte interactions with NPs. This should be ubiquitous for conductive NPs that facilitate charge transfers between cations and anions coadsorbed on NP surfaces, as verified presently by the dependence of the $(BBIB)^{2+}$ SERS feature on the counterions. Moreover, we have unambiguously demonstrated that cation specific effects play a major role during the halide-induced AuNP aggregation, fusion, interaction and ion exchange processes although anion-specific effects, which have been reported before, are also important. Mechanistically, these counterion effects are due to the cooperative and competitive cation and anion binding to AuNPs, and AuNP-facilitated cation and anion interactions. The insights presented herein should be of general significance on NP interfacial interactions with electrolytes.

Notes: This work has been previously published: Perera, G.S.; Yang, G.; Nettles II, C.B.; Perez, F.; Hollis, T.K.; Zhang, D., Counterion Effects on Electrolyte Interactions with Gold Nanoparticles. *J. Phys. Chem. C* **2016**, *120*, 23604-23612.

CHAPTER IV

ION PAIRING AS THE MAIN PATHWAY FOR REDUCING ELECTROSTATIC REPULSION AMONG ORGANOTHIOLATE SELF-ASSEMBLED ON GOLD NANOPARTICLES IN WATER

(Published in *J. Phys. Chem. C* **2016**, *120*, 19878-19884)

4.1 Abstract

Organothiol binding to gold nanoparticles (AuNPs) in water proceeds through a deprotonation pathway in which the sulfur-bound hydrogen (RS-H) atoms are released to solution as protons and the organothiol attach to AuNPs as negatively charged thiolate. The missing puzzle pieces in this mechanism are (i) the significance of electrostatic repulsion among the likely-charged thiolates packed on AuNP surfaces, and (ii) the pathways for the ligand binding system to cope with such electrostatic repulsion. Presented herein are a series of experimental and theoretical evidences that ion pairing, the coadsorption of negatively charged thiolate and positively charged cations, is a main mechanism for the system to reduce the electrostatic repulsion among the thiolate self-assembled onto AuNP surfaces.

4.2 Introduction

The exact mechanism of organothiol binding to gold has been controversial since the early discovery that the organothiol can self-assemble onto gold surfaces.[11,16,39,135,136]

Recent experimental studies demonstrate that organothiol binding to gold nanoparticles (AuNPs) in water proceeds through a deprotonation pathway in which the sulfur-bound hydrogen (RS-H) atoms are released as protons and the organothiols retain on AuNPs as negatively charged thiolate.[17,137-139] While this deprotonation mechanism can be readily verified through simple pH measurements in combination with surface enhanced Raman spectroscopic (SERS) study,[137,140] it also raises new questions that are critical to the comprehensive understanding of organothiol binding to AuNPs. This is because the accumulation of the negatively charged thiolate must increase the electrostatic repulsion among the thiolate self-assembled on AuNPs. The fact that organothiols can densely pack on AuNP surfaces indicates that either the potential energy from electrostatic repulsion is insignificant in comparison to the Au-S bond energy, or the ligand binding system has ways to effectively cope with such electrostatic repulsion.

There are two possible mechanisms for electrolytes to reduce electrostatic repulsion among the charged species at liquid/solid interfaces. The first is the electrical double layer (EDL) formation in which ionic species with opposite charges to ions on solid surface accumulate in a thin layer of solvent immediately surrounding the charged surfaces. This EDL model has been very successful in explaining a wide range of experimental phenomena including the electrical osmotic flow in electrophoresis,[141-143] and diffusion limited current in electrochemistry.[144-146] The second mechanism is the ion paring formation in which the cations and anions are coadsorbed on solid support.[119] The adsorbed cation and anion can be colocalized in the same position or separated on surfaces.

Direct experimental observation of ion pairing has been recently reported for a series of electrolyte binding to gold nanoparticles (AuNPs) in which both the cation and anion of the electrolytes are SERS active.[119] This ion pairing hypothesis explains why electrolyte threshold concentration for inducing AuNP aggregation can be drastically different (by more than three orders of magnitude) from each other. This experimental observation cannot be explained with the EDL theory alone. According to the EDL theory, the electrolyte threshold concentration should be similar for inducing AuNP aggregations.

Reported herein is a combined experimental and computational study of the charge effects on the organothiol binding to AuNPs. The questions we wish to address include 1) the significance of the electrostatic repulsion among the negatively-charged thiolate on AuNP surfaces and 2) the mechanism for the ligand binding system to cope with the electrostatic repulsion. The model organothiols used in this work include ethanethiol (ET), butanethiol (BuT), 1,2-ethanedithiol (EDT) (Figure 4.1). 1,3-bis(3′-butylimidazolium)benzene dichloride salt ((BBIB)Cl_2) is used as a model electrolyte to probe the ion pairing of thiolated AuNPs. Citrate-reduced AuNPs with a nominal diameter of 13 nm were used in this study (Figure 2.3). For the sake of simplicity, the samples are abbreviated with A/(B/C) to represent a three-component mixture in which the two components in the parenthesis are mixed first before the addition of the third component.

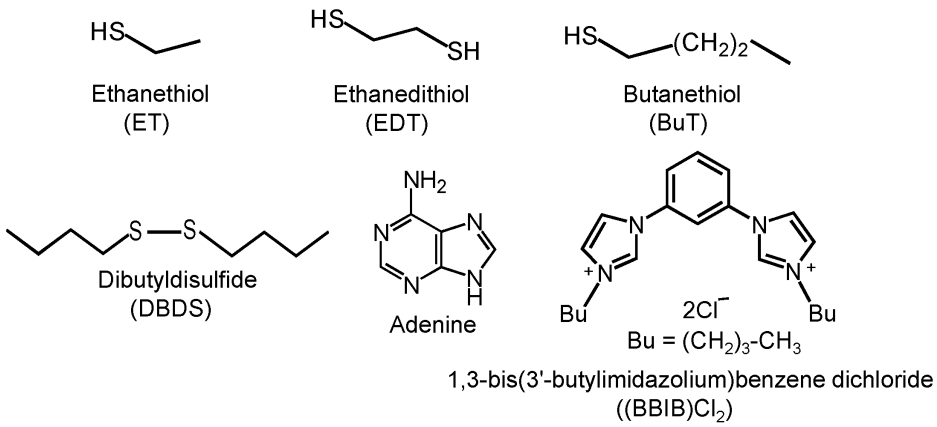

Figure 4.1 Molecular structures of model ligands used in this study.

4.3 Experimental section

4.3.1 Materials and equipment

All chemicals were purchased from Sigma-Aldrich and used as received. $(BBIB)Cl_2$ salt was synthesized according to the previous work.[98] LabRam HR800 confocal Raman microscope was used for Raman and SERS acquisitions with 633 nm laser. pH measurements were obtained using Denver Instrument UB-5 UltraBASIC pH meter. Olis HP 8452 diode array spectrophotometer was used to obtain UV-vis measurements. Nanopure water (18 MΩ-cm) was used to wash the samples and preparation of samples.

4.3.2 AuNP synthesis

AuNPs were synthesized using the same citrate reduction method described in the experimental section in chapter two.

4.3.3 pH measurements of organothiol binding to AuNPs

A 100 mL of as-synthesized AuNPs were centrifuged and the supernatant was replaced with water to remove the excess citrate. This washing step was conducted 2 times and AuNPs were concentrated to 1.0 mL. The washed AuNPs was split into equal volume portions (0.5 mL each) in which the top layer containing the supernatant of the washed AuNPs and the bottom layer containing the AuNPs. 0.5 mL of 10 mM organothiol dissolved in 50% EtOH/water cosolvent was added into each portion and the vortex mixed. The pH measurements of both layers were conducted after overnight sample incubation.

4.3.4 Normal Raman and SERS spectral acquisitions

Normal Raman spectra of organothiols were acquired for both intact organothiol and organothiol dissolved in 1 M NaOH. SERS spectra were acquired for the AuNPs aggregated with pre-defined concentrations of organothiols. All Raman and SERS spectra were taken with laser power before objective of 13 mW and 1.3 mW, respectively.

4.3.5 Competitive ligand binding onto AuNPs

A 0.5 mL of 100 μM $(BBIB)Cl_2$ and 0.5 mL of 100 μM ET was vortex mixed and 1.0 mL of as-synthesized AuNPs was added to this mixture. The vortex mixed AuNP/ligand mixture was incubated overnight allowing the AuNP aggregates to settle to the bottom of the vial and SERS spectra were acquired. In the case of adenine, 0.5 mL of 100 μM $(BBIB)Cl_2$ and 0.5 mL of 100 μM adenine was vortex mixed and this mixture was added to 1.0 mL of as-synthesized AuNPs and the AuNP/ligand mixture was incubated overnight before SERS acquisition. In case of four body mixture, 0.5 mL of

150 μM of each ligand (ET, $(BBIB)Cl_2$, and adenine) was vortex mixed and 1.5 mL of as-synthesized AuNPs was added to that. The SERS spectra were acquired after overnight sample incubation. SERS spectra were acquired for the AuNP aggregates with 200 s acquisition time.

4.3.6 X-ray photoelectron spectroscopy (XPS) analysis

XPS measurements were acquired for the AuNPs aggregated with potassium halide salts deposited on the silicon wafers after the AuNP aggregates were thoroughly washed. The samples were dried with N_2 gas before the XPS measurements. A Thermo Scientific K-Alpha XPS system equipped with a monochromatic X-ray source at 1486.6 eV corresponding to the Al Kα line was used in the XPS analysis. The spot size was 400 μm^2 and the takeoff angle of the collected photoelectrons was 90˚ relative to the sample surface. The pass energy for the acquisition of the survey spectra and high resolution core level spectra were 200 eV and 50 eV, respectively. The average scans for each sample was 20 with a step size of 0.1 eV. All the measurements were performed in the Constant Analyzer Energy mode and "Avantage v5.932" software was used in XPS data analyzing. The XPS measurements were performed by Dr. Felio Perez in University of Memphis.

4.3.7 Computational simulations

Since the exact number of net charges on the AuNPs cannot be determined, a very simple model was used to calculate the electrostatic repulsion among charges adsorbed on Au surfaces. For simplicity, the double layer effect was not considered in the simulations and the medium between charges was treated as water with a relative permittivity of 80.The relative permittivity of a metal cannot be measured at zero

frequency and it was assumed that a perfect conductor has a relative permittivity of one which is the same as a vacuum and the relative permittivity of alkane molecule is about 2.[147]

The calculated results will be different when double layer effect is included and the permittivity of AuNPs and alkane molecule is considered, however, the qualitative conclusion should be still the same. In the simulations, a combined molecular dynamics and steepest gradient decent method was used to find the coordinates of N singly charged species on a 13 nm diameter sphere and then the Columbic repulsion among N charges was calculated using Columbic law. The computational simulations were performed by Dr. Shengli Zou in University of Central Florida.

4.4 Results and discussion

4.4.1 Organothiol binding onto AuNPs

The sulfur-bound hydrogen (RS-H) atoms are released as protons upon organothiol self-assembling onto AuNPs. This conclusion is drawn on the observation that organothiols binding to AuNPs acidifies the ligand binding solutions (Figure 4.2). In this experiment, the as-synthesized AuNPs were centrifugation concentrated and extensively washed with water before mixing with organthiols (Figure 4.2A). The reasons to use washed and concentrated AuNPs, instead of the as-synthesized AuNPs are two folds. The concentrated AuNPs is to ensure that the amount of organothiol adsorption is large enough to produce appreciable solution pH change. The AuNP washing is to reduce excess citrate in the as-synthesized AuNP solution that can act as a buffer to complicate pH measurement. Indeed, even with the extensively washed AuNP aggregates, the amount of proton released to ligand binding solution is slightly more than

half of the amount of organothiol adsorbed onto the AuNPs.[137] One possible reason is that the part of the less-than-expected proton released is that not all the organothiol binding to AuNPs follows the deprotonation pathway. Another possibility is that some of the proton retain adsorbed onto the AuNP surface, either binding to residue citrate that have not been displaced by organothiol, or directly binds to AuNPs as the counterion to the negatively charged thiolate.

The proton detected in AuNP/organothiol solutions must originate from the organothiol deprotonation on AuNPs, but not due to ligand displacement in which adventitious proton adsorbed onto AuNPs are displaced by organothiols. No pH change was observed when dibutyldisulfide (DBDS) onto AuNPs (Figure 4.2B). The lacking of the pH change in the DBDS ligand binding solution excluded the possibility of the proton released to the AuNP solution in the AuNP/ET and AuNP/BuT solution is because of the ligand displacement.

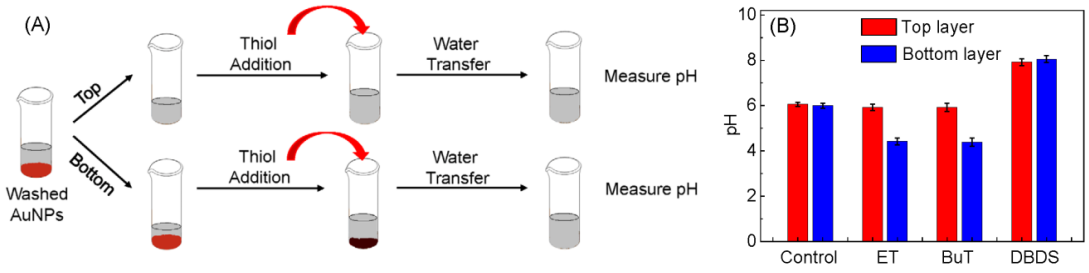

Figure 4.2 (A) Schematic representation for determining pH change induced by organothiol binding onto AuNPs in water. (B) pH change induced by organothiol binding onto AuNPs in water detected by pH meter.

Besides of the pH measurement data, another critical supporting evidence that organothiol binds to AuNPs through deprotonation pathway is the comparison of the

SERS spectra of BuT and DBDS (Figure 4.3). The S-H stretching Raman peak (~2600 cm^{-1}) in neat BuT (Figure 4.3a) is absent in BuT in 1 M NaOH (Figure 4.3b) suggesting that BuT is in thiolate form in 1 M NaOH.[41,148,149] BuT adsorption onto AuNP is evident from the absence of the S-H stretching Raman peak (~2600 cm^{-1}) in the BuT SERS spectra (Figure 4.3c),[41,148,149] while DBDS adsorption onto AuNP is experimentally confirmed by the disappearance of disulfide (S-S) stretching Raman feature in the ~500 cm^{-1} region (Figure 4.3e) compared to neat DBDS in Figure 4.3f .[148,149] These results indicate that the S-H peak in BuT and the S-S peak in DBDS are both cleaved upon their binding to AuNPs (Figure 4.3c and 4.3e).

However, the SERS spectra of the BuT in water is much more similar to the SERS spectrum of BuT dissolved in 1 M NaOH (Figure 4.3c and 4.3d), but different from the SERS spectra of DBDS adsorbed onto AuNP in water (Figure 4.3e), particularly for the spectral feature from 1000 cm^{-1} to 1500 cm^{-1} region. Since BuT in 1 M NaOH is in their thiolate forms before mixing with AuNPs (Figure 4.3b) and therefore they must be adsorbed as thiolates onto AuNPs. The fact that SERS spectra of BuT in water is similar to that of the butanethiolate in 1 M NaOH but different from the disulfide-cleaved DBDS on AuNP strongly indicates that the BuT binds to AuNP as thiolate, but not as the charge neutral radical on AuNPs ($RS^{\bullet}$) as that for DBDS adsorption on AuNPs. These SERS data, in combination with the pH measurement should provide conclusive evidence that the alkanethiol binding to AuNPs proceeds predominantly through the deprotonation pathway. In contrast, if the alkanethiol binding to AuNP is through the radical pathway ($RSH \longrightarrow RS^{\bullet} + H^{\bullet}$), the SERS spectra of BuT in water should be similar to that of the

DBDS, but different from that of BuT in 1 M NaOH, and there should have been no proton releasing upon BuT binding to AuNPs.

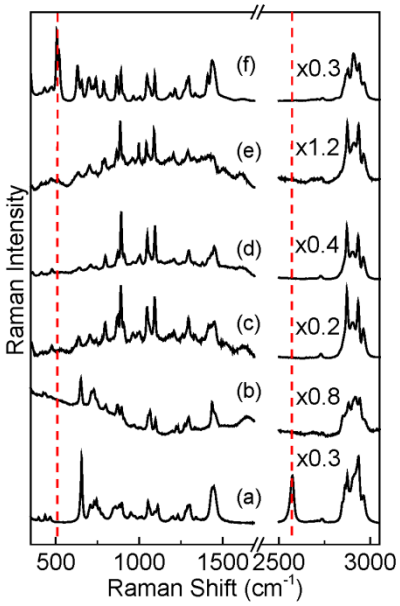

Figure 4.3 (a) The normal Raman spectrum of neat BuT, (b) the normal Raman spectrum of BuT in 1 M NaOH, (c) the SERS spectrum obtained by mixing AuNPs with BuT in water, (d) the SERS spectrum obtained by mixing AuNPs with BuT in 1 M NaOH, (e) the SERS spectrum obtained by mixing AuNPs with DBDS in water, and (f) the normal Raman spectrum of neat DBDS.

Notes: The numbers are the scaling factors for the spectral features in the ~2500-3100 cm^{-1} region in comparison to its spectral features below ~1500 cm^{-1} region. The nominal concentration of BuT in normal Raman and SERS spectra are 5 mM, and 100 µM, respectively. The nominal concentration of DBDS in SERS spectrum is 100 µM. The nominal concentration of AuNPs is 6.5 nM. The red dash lines at ~500 and ~2600 cm^{-1} are correspond to the peak positions of S-S and S-H, respectively.

The fact that alkanethiol adsorption as thiolate indicates that ligand binding system must cope with the electrostatic repulsion among negatively charged thiolate accumulated on AuNPs. It is impossible to experimentally quantify such electrostatic repulsion. In this work, we computed the Coulombic potential energy as a function of the

number of evenly distributed thiolate anions on AuNPs (Figure 4.4) by treating individual thiolate ion as a point charge. The most important learning from data in Figure 4.4 is that without EDL or ion pair formation, it is impossible even for 75 negatively-charged thiolate to pack onto a 13 nm AuNP. This corresponds to an organothiol packing density on AuNPs of 23.4 pmol/cm^2. This is because even at this exceedingly small packing density, the Coulombic potential energy of the ionic species is 650 kJ/mol, which is significantly higher than chemical bonding energy (~250 kJ/mol).

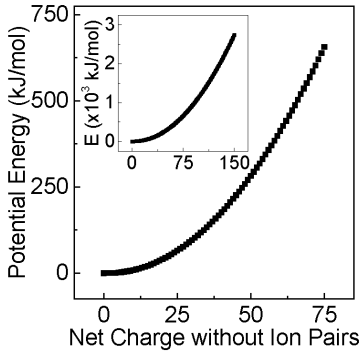

Figure 4.4 Computationally modeled Coulombic potential energy among the singly charge ionic species on AuNP as a function of number of evenly-distributed likely-charged species on a 13 nm AuNP.

The experimental saturation alkanethiol packing density on AuNPs is ~1.7 nmol/cm^2,[41] corresponding to a total of more than 5000 negatively-charged thiolates on a 13 nm AuNPs. Since the Coulombic potential energy calculated for 75 likely-charged species for the AuNP is already higher than covalent bonding energy (Figure 4.4), the ligand binding system must have had a mechanism to reduce the charge repulsions

among the negatively-charged thiolates on AuNPs in order for the thiolate to be stable on AuNPs.

4.4.2 Reduction of electrostatic repulsion among thiolates by ion pairing

Ion pairing, instead of EDL formation is most likely the predominant pathway for the ligand binding system to reduce the electrostatic repulsion among the thiolate ions assembled onto AuNPs. This conclusion is drawn on following theoretical consideration and experimental measurements. The experimental packing density of ~1.7 nmol/cm^2 for organothiol binding to AuNPs, indicating that the footprint of alkanethiol on AuNPs is less than 10 Å^2 on AuNPs.[41] This value is comparative to the cross-section of the methyl groups in alkanethiol chain, leaving no room to accommodate water molecules together with solvated ionic species. This, in combination with the strong hydrophobicity of the hydrocarbon chain of the alkanethiol on AuNP should eliminate the possibility of the formation of EDL immediately surrounding the AuNP surfaces.

Even one assumed that EDL formation on the immediate AuNP surface is possible by water intercalated into the alkylthiol layer, such EDL is inadequate to stabilize thiolate on AuNPs. This conclusion is drawn on the basis of the SERS study of alkanethiolate and alkanedithiolate binding to AuNPs (Figure 4.5). In this experiment, the mono- and di-thiols were first reacted with 1 M NaOH so the RS-H is completely ionized. The latter is confirmed by the Raman measurements in which the relatively strong S-H stretching Raman peak at the ~2600 cm^{-1} region[51,149,150] in the Raman spectra obtained with the intact organothiol totally disappeared in the spectra obtained with their 1 M NaOH solution.

There is an intense disulfide bond (S-S) bond formation for the alkanedithiolate adsorbed onto the AuNP surfaces. This is concluded on the appearance of the disulfide (S-S) stretching feature in the alkanedithiolate SERS spectra at ~500 cm^{-1} region (Figure 4.5B).[149,151,152] Such disulfide bond is totally absent in the ethanethiolate SERS spectrum (Figure 4.5A).

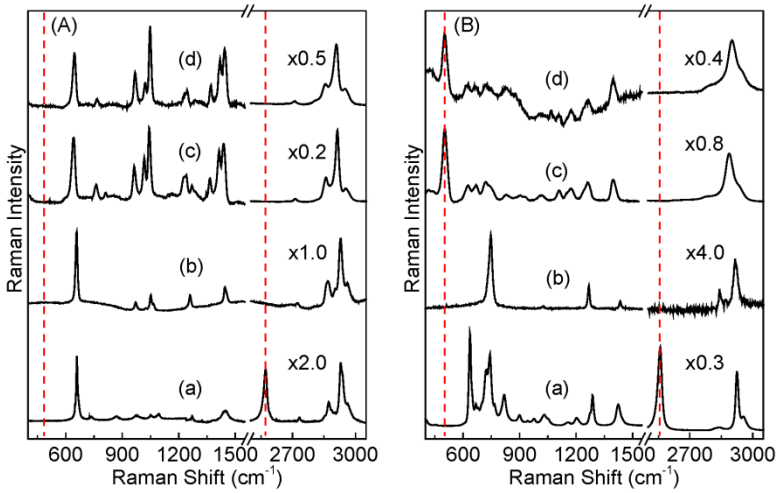

Figure 4.5 Normal Raman and SERS spectra of (A) ET and (B) EDT. (a) and (b) are the normal Raman spectra obtained with the intact analyte and the analyte dissolved in 1 M NaOH, respectively. (c) and (d) are the SERS spectra of the organothiol in water, and 1 M NaOH, respectively.

Notes: The numbers are the scaling factors for the spectral features in the ~2500-3100 cm^{-1} region in comparison to its spectral features below ~1500 cm^{-1} region. The nominal concentration of ET in normal Raman and SERS spectra are 5 mM, and 100 µM, respectively. The nominal concentration of EDT in normal Raman and SERS spectra are 5 mM, and 250 µM, respectively. The nominal concentration of AuNPs is 6.5 nM. The red dashed lines at ~500 and ~2600 cm^{-1} are correspond to the peak positions of S-S and S-H, respectively.

Control experiments indicate that these disulfide bonds are formed after the dithiolates are attached to AuNP surfaces. Without AuNPs, there is no detectable

disulfide formation in sodium dithiolate solution even when the ethanedithiolate was incubated in water for 10 days (Figure 4.6).

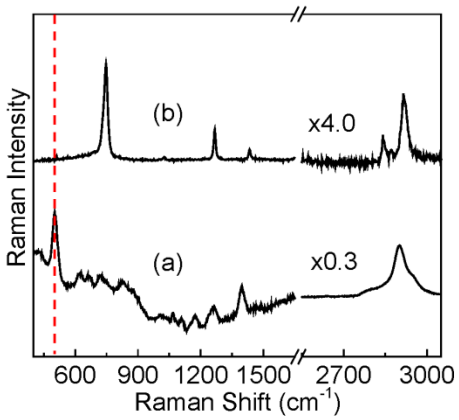

Figure 4.6 (a) SERS spectrum of ethanedithiolate incubated in water for 10 days. (b) Normal Raman spectrum of ethanedithiolate incubated in water for 10 days.

Notes: The numbers are the scaling factors for the spectral features in the ~2500-3100 cm^{-1} region in comparison to its spectral features below ~1500 cm^{-1} region. The nominal concentration of ethanedithiolate in normal Raman and SERS spectra are 5 mM, and 250 μM, respectively. The nominal concentration of AuNPs is 6.5 nM. The red dash line at ~500 cm^{-1} corresponds to the peak position of S-S.

The charge-neutral disulfide bonds are formed primarily between the distal sulfide ions in two dithiolate that are not directly attached to AuNPs. Otherwise, disulfide formation should also be observed in alkylmonothiol adsorbed onto AuNPs. Energetically, the thiolate-to-disulfide conversion on AuNP is driven by the electrostatic repulsion among the likely charged thiolate densely packed on AuNP surfaces. This conclusion is supported by the computational modeling (Figure 4.4) that shows the Coulombic potential energy among monolayer assembled thiolate is significantly higher than covalent binding energy. This thiolate-to-disulfide charge neutralization indicates that EDL formation is inadequate even for protecting the distal thiolate which is close to

water phase. This is in spite of the fact the electrostatic repulsion among the distal thiolate must be smaller than that for the inner thiolate because of the AuNP curvature, and the EDL formation must be more effective in reducing the electrostatic repulsion among the distal thiolate than that for the inner thiolate because of the distal thiolate is in direct contact with water. The fact that only the distal thiolate, but not the inner thiolate is neutralized through the disulfide bond formation on AuNP strongly indicates that ion pairing is the predominant mechanism for the ligand binding system to reduce the electrostatic repulsion among the thiolate directly attached to AuNP surfaces.

Experimental confirmation of ion pairing formation on organothiol-functionalized AuNPs was shown with SERS spectra obtained with AuNPs mixed with ET and $(BBIB)Cl_2$ (Figure 4.7A). $(BBIB)^{2+}$ forms ion pairs with Cl^- on AuNPs in the AuNP/$(BBIB)Cl_2$ sample as indicated by the concurrent appearance of the $(BBIB)^{2+}$ and Cl^- SERS feature obtained with the AuNP/$(BBIB)Cl_2$ sample (Figure 4.7A(a)). This result is consistent with the recent study of $(BBIB)^{2+}$ and halide ion pairing on AuNP surfaces.[119] However, it is the ethanethiolate that pairs with $(BBIB)^{2+}$ when ET is added together with $(BBIB)Cl_2$ onto AuNPs (Figure 4.7A(c)). No significant SERS spectral feature of Cl^- was observed in the AuNP/(ET/$(BBIB)Cl_2$) sample.

The concurrent appearance of $(BBIB)^{2+}$ and ET thiolate SERS features on the thiolated AuNPs is due to the ion pair formation, but not because $(BBIB)^{2+}$ and thiolate has comparable binding affinity to AuNPs. This conclusion is drawn on the experimental data shown in Figure 4.7B that indicate the binding affinity of $(BBIB)^{2+}$ onto AuNPs depends critically on the anion that can be adsorbed onto AuNPs. Without adenine, both $(BBIB)^{2+}$ and Cl^- are coadsorbed onto AuNP surfaces (Figure 4.7A(a)). However, in the

presence of adenine, neither $(BBIB)^{2+}$ nor Cl^- can be detected in the SERS spectrum obtained with the AuNP/((BBIB)Cl_2/adenine) sample (Figure 4.7B(b)). Instead, adenine is the predominant species on the AuNPs. This result indicates that binding affinity of $(BBIB)^{2+}$ and Cl^- ion pair or their individual ions to AuNP is smaller than that for adenine. However, there is no detectable adenine SERS feature in the SERS spectrum of AuNP/((BBIB)Cl_2/ET/adenine). Instead, both $(BBIB)^{2+}$ and ET thiolate SERS features appeared in the SERS spectra obtained with this sample (Figure 4.7B(c)). Since the absence of $(BBIB)^{2+}$ SERS feature in the AuNP/((BBIB)Cl_2/adenine) (Figure 4.7B(b)) excludes the possibility for $(BBIB)^{2+}$ having higher binding affinity to AuNP than adenine, the presence of the $(BBIB)^{2+}$ SERS feature in the AuNP/((BBIB)Cl_2/ET/adenine) sample must be due to the $(BBIB)^{2+}$ and thiolate ion pair formation on AuNPs.

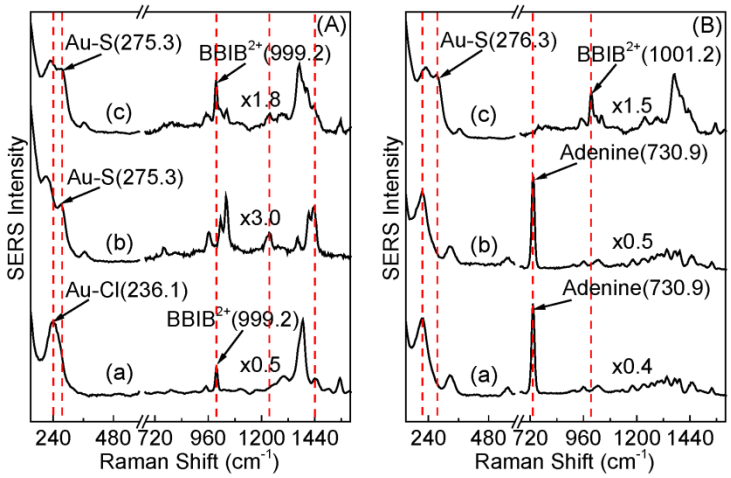

Figure 4.7 (A) SERS spectra of (a) AuNP/$(BBIB)Cl_2$, (b) AuNP/(ET), and (c) AuNP/($(BBIB)Cl_2$/ET). (B) SERS spectra of (a) AuNP/adenine, (b) AuNP/($(BBIB)Cl_2$/adenine), (c) AuNP/($(BBIB)Cl_2$/adenine/ET).

Notes: The numbers are the scaling factors for the spectral features in the ~700-1700 cm^{-1} region in comparison to its spectral features below ~600 cm^{-1} region. The nominal concentrations of AuNPs, ET, and $(BBIB)Cl_2$ are 6.5 nM, 25μM, and 25μM, respectively. The nominal concentrations of AuNPs, adenine, ET, and $(BBIB)Cl_2$ are 6.5 nM, 25μM, 25μM, and 25μM, respectively.

Direct experimental detection of the cations that are coadsorbed with thiolate on AuNPs in organothiol and AuNP mixture is currently impossible (Figure 4.7A(b)). These cations can be protons produced by organothiol deprotonation on AuNP surface or other cations presented in the as-synthesized AuNP solutions before the organothiol addition. Indeed, the as-synthesized AuNPs are rich in ionic adsorbates including citrate and chloride. These ionic species are highly resistant to water washing and ligand displacement.[153] The presence of these anions indicates that the as-synthesized AuNP solution must also contain cations to maintain charge-neutral as a whole. These cations can be alkali metal ions such as sodium from sodium citrate, and proton from $HAuCl_4$, the two reactants used in AuNP synthesis. These cations can be coadsorbed with anions on

AuNPs, confined in the electrical double layer of the anion-attached AuNPs, or dispersed in the AuNP solution in the colloidal AuNP solutions. Compared to proton, the alkali metal ions should be much easier to be coadsorbed onto AuNPs as the counterion to the adsorbed thiolate. This is because of the highest solvation energy of alkali metal is 520 kJ/mol,[154-156] drastically smaller than the solvation energy of proton (1090 kJ/mol).[154,156,157] Unfortunately, however, none of these cations is Raman active, excluding the possibility for SERS detection of thiolate/metal cation ion pairing on AuNPs.

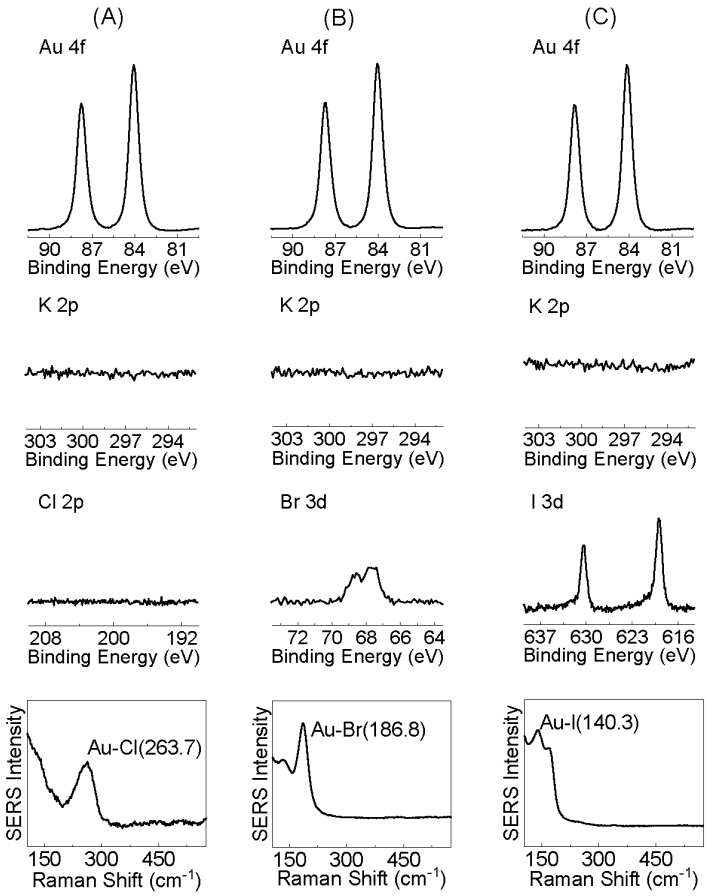

Figure 4.8 Columns indicating the curve-fitted XPS data and SERS spectra of (A) (AuNP/KCl), (B) (AuNP/KBr), and (C) (AuNP/KI).

Notes: 1st and 2nd rows are the XPS data of Au4f and K2p, respectively. 3rd row is the curve-fitted XPS data of halide ions. $Au4f_{7/2}$ peak in all the samples has a binding energy ~84 eV, corresponding to the 0 oxidation state of AuNPs. The peaks of $Br3d_{5/2}$ in (AuNP/KBr), and $I3d_{5/2}$ in (AuNP/KI), at 67.6 and 618.9 eV, respectively, are assigned for the -1 oxidation states of the corresponding halides. All the peak assignments in XPS are performed based on the XPS data in the NIST database. 4th row is the SERS spectra of (AuNP/KCl), (AuNP/KBr), and (AuNP/KI). The nominal concentrations of AuNPs and electrolytes are 6.5 nM, and 1 M, respectively.

Attempt to use XPS to detect the cations co-adsorbed with thiolate is unsuccessful either. It is known that XPS sensitivity differs significantly for different elements. Control experiments conducted with AuNP treated with 1 M potassium halides salts (KCl, KBr, and KI) shows that iodide and bromide give rise to a detectable XPS signal,

but there is no detectable Cl^- and K^+ signal in the XPS spectra (Figure 4.8). This is in spite of the fact the halide adsorption onto AuNP is clearly evidence from the appearance of the Au-X stretching Raman feature in the SERS spectra of the AuNP treated with KX ($X=Cl^-$, Br^-, and I^-) (Figure 4.8) and there must be a cation that is coadsorbed with the anion onto the AuNPs used for the XPS analysis. Nonetheless, the collective experimental data and the computational results shown in this work strongly indicate that the organothiol binding to AuNPs in water follow the deprotonation pathway, and ion pairing must have occurred on thiolated AuNPs in order to stabilize the negatively-charged monolayer-assembled thiolates on AuNP surfaces.

4.5 Conclusions

Organothiol binding to AuNPs in water proceeds through deprotonation pathway in which the organothiols retain on AuNP surface as the negatively charged thiolate ions. Therefore, the organothiol interaction with aqueous AuNPs should be studied as electrolyte binding to AuNP in which the effect of charge repulsion among negatively charged thiolate must be considered in the mechanistic understanding of the energetics associated with the organothiol self-assembly process. The computational and experimental data shown in this work strongly indicates that ion pairing is likely the predominant pathway for the ligand binding system to reduce the electrostatic repulsion. Otherwise, it is impossible for organothiol to be densely packed as intact thiolate on AuNP surfaces. The insights provided in this work are important not only for comprehensive mechanistic understanding of organothiol binding to gold, but also for studying electrolyte interactions with NP surfaces.

Notes: This work has been previously published: Perera, G.S.; Gadogbe, M.; Alahakoon, S.H.; Zhou, Y.; Zou, S.; Perez, F.; Zhang, D., Ion Pairing as the Main Pathway for Reducing Electrostatic Repulsion among Organothiolate Self-assembled on Gold Nanoparticels in Water. *J. Phys. Chem. C* **2016**, *120*, 19878-19884.

REFERENCES

(1) Anker, J. N.; Hall, W. P.; Lyandres, O.; Shah, N. C.; Zhao, J.; Van Duyne, R. P.: Biosensing with Plasmonic Nanosensors. *Nature Mater.* **2008**, *7*, 442-453.

(2) Yang, X.; Yang, M.; Pang, B.; Vara, M.; Xia, Y.: Gold Nanomaterials at Work in Biomedicine. *Chem. Rev.* **2015**, *115*, 10410-10488.

(3) Arvizo, R. R.; Bhattacharyya, S.; Kudgus, R. A.; Giri, K.; Bhattacharya, R.; Mukherjee, P.: Intrinsic Therapeutic Applications of Noble Metal Nanoparticles: Past, Present and Future. *Chem. Soc. Rev.* **2012**, *41*, 2943-2970.

(4) Ghosh, P.; Han, G.; De, M.; Kim, C. K.; Rotello, V. M.: Gold Nanoparticles in Delivery Applications. *Adv. Drug Deliv. Rev.* **2008**, *60*, 1307-1315.

(5) Saha, K.; Agasti, S. S.; Kim, C.; Li, X.; Rotello, V. M.: Gold Nanoparticles in Chemical and Biological Sensing. *Chem. Rev.* **2012**, *112*, 2739-2779.

(6) Cui, C.-H.; Yu, S.-H.: Engineering Interface and Surface of Noble Metal Nanoparticle Nanotubes toward Enhanced Catalytic Activity for Fuel Cell Applications. *Acc. Chem. Res.* **2013**, *46*, 1427-1437.

(7) Jang, Y. H.; Jang, Y. J.; Kim, S.; Quan, L. N.; Chung, K.; Kim, D. H.: Plasmonic Solar Cells: From Rational Design to Mechanism Overview. *Chem. Rev.* **2016**, *116*, 14982-15034.

(8) Atwater, H. A.; Polman, A.: Plasmonics for Improved Photovoltaic Devices. *Nature Mater.* **2010**, *9*, 205-213.

(9) Haran, G.: Single-Molecule Raman Spectroscopy: A Probe of Surface Dynamics and Plasmonic Fields. *Acc. Chem. Res.* **2010**, *43*, 1135-1143.

(10) Eustis, S.; El-Sayed, M. A.: Why Gold Nanoparticles are More Precious than Pretty Gold: Noble Metal Surface Plasmon Resonance and Its Enhancement of the Radiative and Nonradiative Properties of Nanocrystals of Different Shapes. *Chem. Soc. Rev.* **2006**, *35*, 209-217.

(11) Daniel, M.-C.; Astruc, D.: Gold Nanoparticles: Assembly, Supramolecular Chemistry, Quantum-Size-Related Properties, and Applications Toward Biology, Catalysis, and Nanotechnology. *Chem. Rev.* **2004**, *104*, 293-346.

(12) Sardar, R.; Funston, A. M.; Mulvaney, P.; Murray, R. W.: Gold Nanoparticles: Past, Present, and Future. *Langmuir* **2009**, *25*, 13840-13851.

(13) Turkevich, J.; Stevenson, P. C.; Hillier, J.: A Study of the Nucleation and Growth Processes in the Synthesis of Colloidal Gold. *Discuss. Faraday Soc.* **1951**, *11*, 55-75.

(14) Frens, G.: Controlled Nucleation for the Regulation of the Particle Size in Monodisperse Gold Suspensions. *Nature* **1973**, *241*, 20-22.

(15) Brust, M.; Walker, M.; Bethell, D.; Schiffrin, D. J.; Whyman, R.: Synthesis of Thiol-Derivatised Gold Nanoparticles in a Two-Phase Liquid–Liquid System. *J. Chem. Soc, Chem. Commun.* **1994**, 801-802.

(16) Love, J. C.; Estroff, L. A.; Kriebel, J. K.; Nuzzo, R. G.; Whitesides, G. M.: Self-Assembled Monolayers of Thiolates on Metals as a Form of Nanotechnology. *Chem. Rev.* **2005**, *105*, 1103-1170.

(17) Weisbecker, C. S.; Merritt, M. V.; Whitesides, G. M.: Molecular Self-Assembly of Aliphatic Thiols on Gold Colloids. *Langmuir* **1996**, *12*, 3763-3772.

(18) Lin, S.-Y.; Tsai, Y.-T.; Chen, C.-C.; Lin, C.-M.; Chen, C.-h.: Two-Step Functionalization of Neutral and Positively Charged Thiols onto Citrate-Stabilized Au Nanoparticles. *J. Phys. Chem. B* **2004**, *108*, 2134-2139.

(19) Sung, K.-M.; Mosley, D. W.; Peelle, B. R.; Zhang, S.; Jacobson, J. M.: Synthesis of Monofunctionalized Gold Nanoparticles by Fmoc Solid-Phase Reactions. *J. Am. Chem. Soc.* **2004**, *126*, 5064-5065.

(20) Wang, G.; Sun, W.: Optical Limiting of Gold Nanoparticle Aggregates Induced by Electrolytes. *J. Phys. Chem. B* **2006**, *110*, 20901-20905.

(21) Cheng, W.; Dong, S.; Wang, E.: Iodine-Induced Gold Nanoparticle Fusion/Fragmentation/Aggregation and Iodine-Linked Nanostructured Assemblies on a Glass Substrate. *Angew. Chem. Int. Ed.* **2003**, *42*, 449-452.

(22) Liu, Y.; Liu, L.; Guo, R.: Br−-Induced Facile Fabrication of Spongelike Gold/Amino Acid Nanocomposites and Their Applications in Surface-Enhanced Raman Scattering. *Langmuir* **2010**, *26*, 13479-13485.

(23) Perera, G. S.; LaCour, A.; Zhou, Y.; Henderson, K. L.; Zou, S.; Perez, F.; Emerson, J. P.; Zhang, D.: Iodide-Induced Organothiol Desorption and Photochemical Reaction, Gold Nanoparticle (AuNP) Fusion, and SERS Signal Reduction in Organothiol-Containing AuNP Aggregates. *J. Phys. Chem. C* **2015**, *119*, 4261-4267.

(24) Millstone, J. E.; Wei, W.; Jones, M. R.; Yoo, H.; Mirkin, C. A.: Iodide Ions Control Seed-Mediated Growth of Anisotropic Gold Nanoparticles. *Nano Lett.* **2008**, *8*, 2526-2529.

(25) DuChene, J. S.; Niu, W.; Abendroth, J. M.; Sun, Q.; Zhao, W.; Huo, F.; Wei, W. D.: Halide Anions as Shape-Directing Agents for Obtaining High-Quality Anisotropic Gold Nanostructures. *Chem. Mater.* **2012**, *25*, 1392-1399.

(26) Ha, T. H.; Koo, H.-J.; Chung, B. H.: Shape-Controlled Syntheses of Gold Nanoprisms and Nanorods Influenced by Specific Adsorption of Halide Ions. *J. Phys. Chem. C* **2007**, *111*, 1123-1130.

(27) Rai, A.; Singh, A.; Ahmad, A.; Sastry, M.: Role of Halide Ions and Temperature on the Morphology of Biologically Synthesized Gold Nanotriangles. *Langmuir* **2006**, *22*, 736-741.

(28) Kedia, A.; Kumar, P. S.: Halide Ion Induced Tuning and Self-Organization of Gold Nanostars. *RSC Adv.* **2014**, *4*, 4782-4790.

(29) Zhang, Z.; Li, H.; Zhang, F.; Wu, Y.; Guo, Z.; Zhou, L.; Li, J.: Investigation of Halide-Induced Aggregation of Au Nanoparticles into Spongelike Gold. *Langmuir* **2014**, *30*, 2648-2659.

(30) Yu, Y.; Gu, L.; Lang, X.; Zhu, C.; Fujita, T.; Chen, M.; Maier, J.: Li Storage in 3D Nanoporous Au- Supported Nanocrystalline Tin. *Adv. Mater.* **2011**, *23*, 2443-2447.

(31) Wei, Q.; Zhao, Y.; Xu, C.; Wu, D.; Cai, Y.; He, J.; Li, H.; Du, B.; Yang, M.: Nanoporous Gold Film Based Immunosensor for Label-Free Detection of Cancer Biomarker. *Biosens. Bioelec.* **2011**, *26*, 3714-3718.

(32) Wittstock, A.; Wichmann, A.; Baumer, M.: Nanoporous Gold as a Platform for a Building Block Catalyst. *ACS Catal.* **2012**, *2*, 2199-2215.

(33) Davis, A.; Tran, T.: Gold Dissolution in Iodide Electrolytes. *Hydrometallurgy* **1991**, *26*, 163-177.

(34) Daniel, W. L.; Han, M. S.; Lee, J.-S.; Mirkin, C. A.: Colorimetric Nitrite and Nitrate Detection with Gold Nanoparticle Probes and Kinetic End Points. *J. Am. Chem. Soc.* **2009**, *131*, 6362-6363.

(35) Ansar, S. M.; Ameer, F. S.; Hu, W.; Zou, S.; Pittman Jr, C. U.; Zhang, D.: Removal of Molecular Adsorbates on Gold Nanoparticles using Sodium Borohydride in Water. *Nano Lett.* **2013**, *13*, 1226-1229.

(36) Ansar, S. M.; Perera, G. S.; Ameer, F. S.; Zou, S.; Pittman Jr, C. U.; Zhang, D.: Desulfurization of Mercaptobenzimidazole and Thioguanine on Gold Nanoparticles using Sodium Borohydride in Water at Room Temperature. *J. Phys. Chem. C* **2013**, *117*, 13722-13729.

(37) Zhang, Z.; Wu, Y.: $NaBH_4$-Induced Assembly of Immobilized Au Nanoparticles into Chainlike Structures on a Chemically Modified Glass Surface. *Langmuir* **2011**, *27*, 9834-9842.

(38) Zhang, Z.; Chen, Z.; Wang, S.; Qu, C.; Chen, L.: On-Site Visual Detection of Hydrogen Sulfide in Air Based on Enhancing the Stability of Gold Nanoparticles. *ACS Appl. Mater. Interfaces* **2014**, *6*, 6300-6307.

(39) Häkkinen, H.: The Gold-Sulfur Interface at the Nanoscale. *Nature Chem.* **2012**, *4*, 443-455.

(40) Weeraman, C.; Yatawara, A. K.; Bordenyuk, A. N.; Benderskii, A. V.: Effect of Nanoscale Geometry on Molecular Conformation: Vibrational Sum-Frequency Generation of Alkanethiols on Gold Nanoparticles. *J. Am. Chem. Soc.* **2006**, *128*, 14244-14245.

(41) Ansar, S. M.; Gadogbe, M.; Siriwardana, K.; Howe, J. Y.; Dogel, S.; Hosseinkhannazer, H.; Collier, W. E.; Rodriguez, J.; Zou, S.; Zhang, D.: Dispersion Stability, Ligand Structure and Conformation, and SERS Activities of 1-Alkanethiol Functionalized Gold and Silver Nanoparticles. *J. Phys. Chem. C* **2014**, *118*, 24925-24934.

(42) Levin, C. S.; Janesko, B. G.; Bardhan, R.; Scuseria, G. E.; Hartgerink, J. D.; Halas, N. J.: Chain-Length-Dependent Vibrational Resonances in Alkanethiol Self-Assembled Monolayers Observed on Plasmonic Nanoparticle Substrates. *Nano Lett.* **2006**, *6*, 2617-2621.

(43) Chen, C.-F.; Tzeng, S.-D.; Chen, H.-Y.; Lin, K.-J.; Gwo, S.: Tunable Plasmonic Response from Alkanethiolate-Stabilized Gold Nanoparticle Superlattices: Evidence of Near-Field Coupling. *J. Am. Chem. Soc.* **2008**, *130*, 824-826.

(44) Ghosh, S. K.; Pal, T.: Interparticle Coupling Effect on the Surface Plasmon Resonance of Gold Nanoparticles: From Theory to Applications. *Chem. Rev.* **2007**, *107*, 4797-4862.

(45) Kelly, K. L.; Coronado, E.; Zhao, L. L.; Schatz, G. C.: The Optical Properties of Metal Nanoparticles: The Influence of Size, Shape, and Dielectric Environment. *J. Phys. Chem. B* **2003**, *107*, 668-677.

(46) Willets, K. A.; Van Duyne, R. P.: Localized Surface Plasmon Resonance Spectroscopy and Sensing. *Annu. Rev. Phys. Chem.* **2007**, *58*, 267-297.

(47) Miller, M. M.; Lazarides, A. A.: Sensitivity of Metal Nanoparticle Surface Plasmon Resonance to the Dielectric Environment. *J. Phys. Chem. B* **2005**, *109*, 21556-21565.

(48) Mulvaney, P.: Surface Plasmon Spectroscopy of Nanosized Metal Particles. *Langmuir* **1996**, *12*, 788-800.

(49) Doane, T. L.; Chuang, C.-H.; Hill, R. J.; Burda, C.: Nanoparticle ζ-Potentials. *Acc. Chem. Res.* **2011**, *45*, 317-326.

(50) Badia, A.; Cuccia, L.; Demers, L.; Morin, F.; Lennox, R. B.: Structure and Dynamics in Alkanethiolate Monolayers Self-Assembled on Gold Nanoparticles: A DSC, FT-IR, and Deuterium NMR Study. *J. Am. Chem. Soc.* **1997**, *119*, 2682-2692.

(51) Aryal, S.; B.K.C, R.; Dharmaraj, N.; Bhattarai, N.; Kim, C. H.; Kim, H. Y.: Spectroscopic Identification of S-Au Interaction in Cysteine Capped Gold Nanoparticles. *Spectrochim. Acta A: Mol. Biomol. Spec.* **2006**, *63*, 160-163.

(52) Zhang, P.; Sham, T.: X-Ray Studies of the Structure and Electronic Behavior of Alkanethiolate-Capped Gold Nanoparticles: The Interplay of Size and Surface Effects. *Phys. Rev. Lett.* **2003**, *90*, 245502.

(53) Bourg, M.-C.; Badia, A.; Lennox, R. B.: Gold−Sulfur Bonding in 2D and 3D Self-Assembled Monolayers: XPS Characterization. *J. Phys. Chem. B* **2000**, *104*, 6562-6567.

(54) Hasan, M.; Bethell, D.; Brust, M.: The Fate of Sulfur-Bound Hydrogen on Formation of Self-Assembled Thiol Monolayers on Gold: 1H NMR Spectroscopic Evidence from Solutions of Gold Clusters. *J. Am. Chem. Soc.* **2002**, *124*, 1132-1133.

(55) Smith, A. M.; Marbella, L. E.; Johnston, K. A.; Hartmann, M. J.; Crawford, S. E.; Kozycz, L. M.; Seferos, D. S.; Millstone, J. E.: Quantitative Analysis of Thiolated Ligand Exchange on Gold Nanoparticles Monitored by 1H NMR Spectroscopy. *Anal. Chem.* **2015**, *87*, 2771-2778.

(56) Wang, M.; Zhang, Z.; He, J.: A SERS Study on the Assembly Behavior of Gold Nanoparticles at the Oil/Water Interface. *Langmuir* **2015**, *31*, 12911-12919.

(57) Tong, L.; Zhu, T.; Liu, Z.: Approaching the Electromagnetic Mechanism of Surface-Enhanced Raman Scattering: From Self-Assembled Arrays to Individual Gold Nanoparticles. *Chem. Soc. Rev.* **2011**, *40*, 1296-1304.

(58) Haynes, C. L.; McFarland, A. D.; Duyne, R. P. V.: Surface-Enhanced Raman Spectroscopy. *Anal. Chem.* **2005**, *77*, 338 A-346 A.

(59) Kneipp, K.; Kneipp, H.; Manoharan, R.; Hanlon, E. B.; Itzkan, I.; Dasari, R. R.; Feld, M. S.: Extremely Large Enhancement Factors in Surface-Enhanced Raman Scattering for Molecules on Colloidal Gold Clusters. *Appl. Spec.* **1998**, *52*, 1493-1497.

(60) Le Ru, E.; Blackie, E.; Meyer, M.; Etchegoin, P. G.: Surface Enhanced Raman Scattering Enhancement Factors: A Comprehensive Study. *J. Phys. Chem. C* **2007**, *111*, 13794-13803.

(61) Nie, S.; Emory, S. R.: Probing Single Molecules and Single Nanoparticles by Surface-Enhanced Raman Scattering. *Science* **1997**, *275*, 1102-1106.

(62) Kneipp, K.; Kneipp, H.; Kartha, V. B.; Manoharan, R.; Deinum, G.; Itzkan, I.; Dasari, R. R.; Feld, M. S.: Detection and Identification of a Single DNA Base Molecule using Surface-Enhanced Raman Scattering (SERS). *Phys. Rev. E* **1998**, *57*, R6281.

(63) Kleinman, S. L.; Ringe, E.; Valley, N.; Wustholz, K. L.; Phillips, E.; Scheidt, K. A.; Schatz, G. C.; Van Duyne, R. P.: Single-Molecule Surface-Enhanced Raman Spectroscopy of Crystal Violet Isotopologues: Theory and Experiment. *J. Am. Chem. Soc.* **2011**, *133*, 4115-4122.

(64) Lombardi, J. R.; Birke, R. L.; Lu, T.; Xu, J.: Charge- Transfer Theory of Surface Enhanced Raman Spectroscopy: Herzberg–Teller Contributions. *J. Chem. Phys.* **1986**, *84*, 4174-4180.

(65) Arenas, J. F.; Fernandez, D. J.; Soto, J.; Lopez-Tocon, I.; Otero, J. C.: Role of the Electrode Potential in the Charge-Transfer Mechanism of Surface-Enhanced Raman Scattering. *J. Phys. Chem. B* **2003**, *107*, 13143-13149.

(66) Etchegoin, P.; Cohen, L.; Hartigan, H.; Brown, R.; Milton, M.; Gallop, J.: Electromagnetic Contribution to Surface Enhanced Raman Scattering Revisited. *J. Chem. Phys.* **2003**, *119*, 5281-5289.

(67) Boyd, G.; Rasing, T.; Leite, J.; Shen, Y.: Local-Field Enhancement on Rough Surfaces of Metals, Semimetals, and Semiconductors with the use of Optical Second-Harmonic Generation. *Phys. Rev. B* **1984**, *30*, 519.

(68) Campion, A.; Kambhampati, P.: Surface-Enhanced Raman Scattering. *Chem. Soc. Rev.* **1998**, *27*, 241-250.

(69) Farcau, C.; Astilean, S.: Mapping the SERS Efficiency and Hot-Spots Localization on Gold Film Over Nanospheres Substrates. *J. Phys. Chem. C* **2010**, *114*, 11717-11722.

(70) Schwartzberg, A. M.; Grant, C. D.; Wolcott, A.; Talley, C. E.; Huser, T. R.; Bogomolni, R.; Zhang, J. Z.: Unique Gold Nanoparticle Aggregates as a Highly Active Surface-Enhanced Raman Scattering Substrate. *J. Phys. Chem. B* **2004**, *108*, 19191-19197.

(71) Wustholz, K. L.; Henry, A.-I.; McMahon, J. M.; Freeman, R. G.; Valley, N.; Piotti, M. E.; Natan, M. J.; Schatz, G. C.; Duyne, R. P. V.: Structure−Activity Relationships in Gold Nanoparticle Dimers and Trimers for Surface-Enhanced Raman Spectroscopy. *J. Am. Chem. Soc.* **2010**, *132*, 10903-10910.

(72) Chen, G.; Wang, Y.; Yang, M.; Xu, J.; Goh, S. J.; Pan, M.; Chen, H.: Measuring Ensemble-Averaged Surface-Enhanced Raman Scattering in the Hotspots of Colloidal Nanoparticle Dimers and Trimers. *J. Am. Chem. Soc.* **2010**, *132*, 3644-3645.

(73) Kim, T.; Lee, K.; Gong, M.-s.; Joo, S.-W.: Control of Gold Nanoparticle Aggregates by Manipulation of Interparticle Interaction. *Langmuir* **2005**, *21*, 9524-9528.

(74) Helmholtz, H. v.: Ueber einige Gesetze der Vertheilung elektrischer Ströme in körperlichen Leitern mit Anwendung auf die thierisch elektrischen Versuche. *Annalen der Physik* **1853**, *165*, 211-233.

(75) Gouy, M.: Sur la constitution de la charge électrique à la surface d'un électrolyte. *J. Phys. Theor. Appl.* **1910**, *9*, 457-468.

(76) Chapman, D. L.: LI. A Contribution to the Theory of Electrocapillarity. *The London, Edinburgh, and Dublin Philosophical Magazine and Journal of Science* **1913**, *25*, 475-481.

(77) Stern, O.: Zur theorie der elektrolytischen doppelschicht. *Berichte der Bunsengesellschaft für physikalische Chemie* **1924**, *30*, 508-516.

(78) Pfeiffer, C.; Rehbock, C.; Hühn, D.; Carrillo-Carrion, C.; de Aberasturi, D. J.; Merk, V.; Barcikowski, S.; Parak, W. J.: Interaction of Colloidal Nanoparticles with Their Local Environment: The (Ionic) Nanoenvironment Around Nanoparticles is Different from Bulk and Determines the Physico-Chemical Properties of the Nanoparticles. *J. Royal Soc. Interface* **2014**, *11*, 20130931.

(79) Verwey, E. J. W.; Overbeek, J. T. G.: *Theory of the Stability of Lyophobic Colloids* Amsterdam: Elsevier **1948**.

(80) Sze, A.; Erickson, D.; Ren, L.; Li, D.: Zeta-Potential Measurement using the Smoluchowski Equation and the Slope of the Current–Time Relationship in Electroosmotic Flow. *J. Col. Interface Sci.* **2003**, *261*, 402-410.

(81) Ninham, B.: On Progress in Forces since the DLVO Theory. *Adv. Colloid Interface Sci.* **1999**, *83*, 1-17.

(82) Marcus, Y.; Hefter, G.: Ion Pairing. *Chem. Rev.* **2006**, *106*, 4585-4621.

(83) Cecchi, T.: Ion Pairing Chromatography. *Crit. Rev. Anal. Chem.* **2008**, *38*, 161-213.

(84) Anderson, K. M.; Esadze, A.; Manoharan, M.; Bruschweiler, R.; Gorenstein, D. G.; Iwahara, J.: Direct Observation of the Ion-Pair Dynamics at a Protein–DNA Interface by NMR Spectroscopy. *J. Am. Chem. Soc.* **2013**, *135*, 3613-3619.

(85) Lacour, J.; Moraleda, D.: Chiral Anion-Mediated Asymmetric Ion Pairing Chemistry. *Chem. Commun.* **2009**, 7073-7089.

(86) Macchioni, A.: Ion Pairing in Transition-Metal Organometallic Chemistry. *Chem. Rev.* **2005**, *105*, 2039-2074.

(87) Houk, R. J.; Monzingo, A.; Anslyn, E. V.: Electrophilic Coordination Catalysis: A Summary of Previous Thought and a New Angle of Analysis. *Acc. Chem. Res.* **2008**, *41*, 401-410.

(88) Anderson, M. A.; Ogbay, B.; Arimoto, R.; Sha, W.; Kisselev, O. G.; Cistola, D. P.; Marshall, G. R.: Relative Strength of Cation-π vs Salt-Bridge Interactions: The Gtα (340− 350) Peptide/Rhodopsin System. *J. Am. Chem. Soc.* **2006**, *128*, 7531-7541.

(89) Chan, L.; Smid, J.: Contact and Solvent-Separated Ion Pairs of Carbanions. V. The Role of Solvent Structure in Alkali Ion Solvation. *J. Am. Chem. Soc.* **1968**, *90*, 4654-4661.

(90) Bakker, H. J.: Water Dynamics: Ion-Ing Out the Details. *Nature Chem.* **2009**, *1*, 24-25.

(91) No, K. T.; Nam, K.-Y.; Scheraga, H. A.: Stability of Like and Oppositely Charged Organic Ion Pairs in Aqueous Solution. *J. Am. Chem. Soc.* **1997**, *119*, 12917-12922.

(92) Antonio, M. R.; Nyman, M.; Anderson, T. M.: Direct Observation of Contact Ion Pair Formation in Aqueous Solution. *Angew. Chem.* **2009**, *121*, 6252-6256.

(93) Chorny, I.; Dill, K. A.; Jacobson, M. P.: Surfaces Affect Ion Pairing. *J. Phys. Chem. B* **2005**, *109*, 24056-24060.

(94) Howes, B. D.; Guerrini, L.; Sanchez-Cortes, S.; Marzocchi, M. P.; Garcia Ramos, J. V.; Smulevich, G.: The Influence of pH and Anions on the Adsorption Mechanism of Rifampicin on Silver Colloids. *J. Raman Spec.* **2007**, *38*, 859-864.

(95) Šloufová, I.; Vlčková, B.; Procházka, M.; Svoboda, J.; Vohlídal, J.: Comparison of SERRS and RRS Excitation Profiles of [Fe (tpy) 2] 2+(tpy= 2, 2': 6', 2''-terpyridine) Supported by DFT Calculations: Effect of the Electrostatic Bonding to Chloride-Modified Ag Nanoparticles on its Vibrational and Electronic Structure. *J. Raman Spec.* **2014**, *45*, 338-348.

(96) Li, S.; Pedano, M. L.; Chang, S.-H.; Mirkin, C. A.; Schatz, G. C.: Gap Structure Effects on Surface-Enhanced Raman Scattering Intensities for Gold Gapped Rods. *Nano Lett.* **2010**, *10*, 1722-1727.

(97) Alvarez Puebla, R. A.; Liz-Marzán, L. M.: SERS-Based Diagnosis and Biodetection. *Small* **2010**, *6*, 604-610.

(98) Clark, W. D.; Cho, J.; Valle, H. U.; Hollis, T. K.; Valente, E. J.: Metal and Halogen Dependence of the Rate Effect in Hydroamination/Cyclization of Unactivated Aminoalkenes: Synthesis, Characterization, and Catalytic Rates of CCC-NHC Hafnium and Zirconium Pincer Complexes. *J. Organometal. Chem.* **2014**, *751*, 534-540.

(99) Zhao, W.; Chiuman, W.; Lam, J. C.; McManus, S. A.; Chen, W.; Cui, Y.; Pelton, R.; Brook, M. A.; Li, Y.: DNA Aptamer Folding on Gold Nanoparticles: From Colloid Chemistry to Biosensors. *J. Am. Chem. Soc.* **2008**, *130*, 3610-3618.

(100) Hurst, S. J.; Lytton-Jean, A. K.; Mirkin, C. A.: Maximizing DNA Loading on a Range of Gold Nanoparticle Sizes. *Anal. Chem.* **2006**, *78*, 8313-8318.

(101) Svensson, P. H.; Rosdahl, J.; Kloo, L.: Metal Iodides in Polyiodide Networks—The Structural Chemistry of Complex Gold Iodides with Excess Iodine. *Chem.–Eur. J.* **1999**, *5*, 305-311.

(102) Tang, Z.; Litvinchuk, A.; Lee, H.-G.; Guloy, A. M.: Crystal Structure and Vibrational Spectra of a New Viologen Gold (I) Iodide. *Inorg. Chem.* **1998**, *37*, 4752-4753.

(103) Nikoobakht, B.; El-Sayed, M. A.: Surface-Enhanced Raman Scattering Studies on Aggregated Gold Nanorods. *J. Phys. Chem. A* **2003**, *107*, 3372-3378.

(104) Pan, P.; Wood, S. A.: Gold Bromide Complexes in Acidic Aqueous Solutions from 25° to 300° C. A Laser Raman Spectroscopic Study. *J. Solution Chem.* **1993**, *22*, 163-172.

(105) Gao, P.; Weaver, M. J.: Metal-Adsorbate Vibrational Frequencies as a Probe of Surface Bonding: Halides and Pseudohalides at Gold Electrodes. *J. Phys. Chem.* **1986**, *90*, 4057-4063.

(106) Moskovits, M.; Suh, J.: Surface Selection Rules for Surface-Enhanced Raman Spectroscopy: Calculations and Application to the Surface-Enhanced Raman Spectrum of Phthalazine on Silver. *J. Phys. Chem.* **1984**, *88*, 5526-5530.

(107) Brown, J. R.; Schwerdtfeger, P.; Schröder, D.; Schwarz, H.: Experimental and Theoretical Studies of Diatomic Gold Halides. *J. Am. Soc. Mass Spec.* **2002**, *13*, 485-492.

(108) Dubois, L. H.; Nuzzo, R. G.: Synthesis, Structure, and Properties of Model Organic Surfaces. *Ann. Rev. Phys. Chem.* **1992**, *43*, 437-463.

(109) Reincke, F.; Hickey, S. G.; Kegel, W. K.; Vanmaekelbergh, D.: Spontaneous Assembly of a Monolayer of Charged Gold Nanocrystals at the Water/Oil Interface. *Angew. Chem. Int. Ed.* **2004**, *43*, 458-462.

(110) Jungwirth, P.: Ion Pairing: From Water Clusters to the Aqueous Bulk. *J. Phys. Chem. B* **2014**, *118*, 10333-10334.

(111) Brandes, E.; Stage, C.; Motschmann, H.; Rieder, J.; Buchner, R.: Is Surface Layering of Aqueous Alkali Halides Determined by Ion Pairing in the Bulk Solution? *J. Chem. Phys.* **2014**, *141*, 18C509.

(112) Bian, H.-t.; Feng, R.-r.; Guo, Y.; Wang, H.-f.: Specific Na+ and K+ Cation Effects on the Interfacial Water Molecules at the Air/Aqueous Salt Solution Interfaces Probed with Nonresonant Second Harmonic Generation. *J. Chem. Phys.* **2009**, *130*, 134709.

(113) Dykman, L.; Khlebtsov, N.: Gold Nanoparticles in Biomedical Applications: Recent Advances and Perspectives. *Chem. Soc. Rev.* **2012**, *41*, 2256-2282.

(114) Aryal, S.; KC, R. B.; Bhattarai, N.; Kim, C. K.; Kim, H. Y.: Study of Electrolyte Induced Aggregation of Gold Nanoparticles Capped by Amino Acids. *J. Col. Interface Sci.* **2006**, *299*, 191-197.

(115) Grahame, D. C.: The Electrical Double Layer and the Theory of Electrocapillarity. *Chem. Rev.* **1947**, *41*, 441-501.

(116) Mayergoyz, I. D.; Fredkin, D. R.; Zhang, Z.: Electrostatic (Plasmon) Resonances in Nanoparticles. *Phys. Rev. B* **2005**, *72*, 155412.

(117) Ohshima, H.; Healy, T. W.; White, L. R.: Accurate Analytic Expressions for the Surface Charge Density/Surface Potential Relationship and Double-Layer Potential Distribution for a Spherical Colloidal Particle. *J. Col. Interface Sci.* **1982**, *90*, 17-26.

(118) White, L. R.: Approximate Analytic Solution of the Poisson–Boltzmann Equation for a Spherical Colloidal Particle. *J. Chem. Soc., Faraday Trans. 2: Mole. Chem. Phys.* **1977**, *73*, 577-596.

(119) Perera, G. S.; Nettles, C. B.; Zhou, Y.; Zou, S.; Hollis, T. K.; Zhang, D.: Direct Observation of Ion Pairing at the Liquid/Solid Interfaces by Surface Enhanced Raman Spectroscopy. *Langmuir* **2015**, *31*, 8998-9005.

(120) Le Ru, E. C.; Etchegoin, P. G.: Single-Molecule Surface-Enhanced Raman Spectroscopy. *Annu. Rev. Phys. Chem.* **2012**, *63*, 65-87.

(121) Kneipp, K.; Kneipp, H.; Itzkan, I.; Dasari, R. R.; Feld, M. S.: Ultrasensitive Chemical Analysis by Raman Spectroscopy. *Chem. Rev.* **1999**, *99*, 2957-2976.

(122) Merk, V.; Rehbock, C.; Becker, F.; Hagemann, U.; Nienhaus, H.; Barcikowski, S.: In Situ Non-DLVO Stabilization of Surfactant-Free, Plasmonic Gold Nanoparticles: Effect of Hofmeister's Anions. *Langmuir* **2014**, *30*, 4213-4222.

(123) Gadogbe, M.; Ansar, S. M.; He, G.; Collier, W. E.; Rodriguez, J.; Liu, D.; Chu, I.-W.; Zhang, D.: Determination of Colloidal Gold Nanoparticle Surface Areas, Concentrations, and Sizes Through Quantitative Ligand Adsorption. *Anal. Bioanal. Chem.* **2013**, *405*, 413-422.

(124) Ansar, S. M.; Haputhanthri, R.; Edmonds, B.; Liu, D.; Yu, L.; Sygula, A.; Zhang, D.: Determination of the Binding Affinity, Packing, and Conformation of Thiolate and Thione Ligands on Gold Nanoparticles. *J. Phys. Chem. C* **2010**, *115*, 653-660.

(125) Lyklema, J.: Simple Hofmeister Series. *Chem. Phys. Lett.* **2009**, *467*, 217-222.

(126) Mirza, J.; Smith, S. R.; Baron, J. Y.; Choi, Y.; Lipkowski, J.: A SERS Characterization of the Stability of Polythionates at the Gold–Electrolyte Interface. *Surf. Sci.* **2015**, *631*, 196-206.

(127) Gadgil, B.; Damlin, P.; Viinikanoja, A.; Heinonen, M.; Kvarnström, C.: One-Pot Synthesis of an Au/Au 2 S Viologen Hybrid Nanocomposite for Efficient Catalytic Applications. *J. Mater. Chem. A* **2015**, *3*, 9731-9737.

(128) Gledhill, J.; Malan, G. M.: The Solubilities of Sparingly Soluble Salts in Water. I. The Solubility of Silver Chloride at 25° C. *Trans. Faraday Soc.* **1952**, *48*, 258-262.

(129) Davies, C.; Jones, A.: The Precipitation of Silver Chloride from Aqueous Solutions. Part I. *Discuss. Faraday Soc.* **1949**, *5*, 103-111.

(130) Sugimoto, T.; Shiba, F.: Spontaneous Nucleation of Monodisperse Silver Halide Particles from Homogeneous Gelatin Solution II: Silver Bromide. *Col. Surf. A: Physicochem. Eng. Asp.* **2000**, *164*, 205-215.

(131) Firsching, F. H.: Selective Precipitation of Silver Halides from Homogeneous Solution. Separation of Iodide, Bromide, and Chloride using Volatilization of Ammonia. *Anal. Chem.* **1960**, *32*, 1876-1878.

(132) Mladenovic, I. L.; Kegel, W. K.; Bomans, P.; Frederik, P. M.: Observation of Equilibrium, Nanometer-Sized Clusters of Silver Iodide in Aqueous Solutions. *J. Phys. Chem. B* **2003**, *107*, 5717-5722.

(133) Chen, W.-Y.; Lan, G.-Y.; Chang, H.-T.: Use of Fluorescent DNA-Templated Gold/Silver Nanoclusters for the Detection of Sulfide Ions. *Anal. Chem.* **2011**, *83*, 9450-9455.

(134) Goia, D. V.: Preparation and Formation Mechanisms of Uniform Metallic Particles in Homogeneous Solutions. *J. Mater. Chem.* **2004**, *14*, 451-458.

(135) Pensa, E.; Cortes, E.; Corthey, G. n.; Carro, P.; Vericat, C.; Fonticelli, M. H.; Benitez, G.; Rubert, A. A.; Salvarezza, R. C.: The Chemistry of the Sulfur–Gold Interface: In Search of a Unified Model. *Acc. Chem. Res.* **2012**, *45*, 1183-1192.

(136) Vericat, C.; Vela, M.; Benitez, G.; Carro, P.; Salvarezza, R.: Self-Assembled Monolayers of Thiols and Dithiols on Gold: New Challenges for a Well-Known System. *Chem. Soc. Rev.* **2010**, *39*, 1805-1834.

(137) Ansar, S. M.; Perera, G. S.; Jiang, D.; Holler, R. A.; Zhang, D.: Organothiols Self-Assembled onto Gold: Evidence for Deprotonation of the Sulfur-Bound Hydrogen and Charge Transfer from Thiolate. *J. Phys. Chem. C* **2013**, *117*, 8793-8798.

(138) Bain, C. D.; Biebuyck, H. A.; Whitesides, G. M.: Comparison of Self-Assembled Monolayers on Gold: Coadsorption of Thiols and Disulfides. *Langmuir* **1989**, *5*, 723-727.

(139) Murty, K.; Venkataramanan, M.; Pradeep, T.: Self-Assembled Monolayers of 1, 4-Benzenedimethanethiol on Polycrystalline Silver and Gold Films: An Investigation of Structure, Stability, Dynamics, and Reactivity. *Langmuir* **1998**, *14*, 5446-5456.

(140) Karunanayake, A. G.; Gunatilake, S. R.; Ameer, F. S.; Gadogbe, M.; Smith, L.; Mlsna, D.; Zhang, D.: Undergraduate Laboratory Experiment Modules for Probing Gold Nanoparticle Interfacial Phenomena. *J. Chem. Edu.* **2015**, *92*, 1924-1927.

(141) Gillespie, D.; Pennathur, S.: Separation of Ions in Nanofluidic Channels with Combined Pressure-Driven and Electro-Osmotic Flow. *Anal. Chem.* **2013**, *85*, 2991-2998.

(142) Hsu, J.-P.; Hsu, W.-L.; Liu, K.-L.: Diffusiophoresis of a Charge-Regulated Sphere Along the Axis of an Uncharged Cylindrical Pore. *Langmuir* **2010**, *26*, 8648-8658.

(143) Joly, L.; Ybert, C.; Trizac, E.; Bocquet, L.: Hydrodynamics within the Electric Double Layer on Slipping Surfaces. *Phys. Rev. Lett.* **2004**, *93*, 257805.

(144) Hauch, A.; Georg, A.: Diffusion in the Electrolyte and Charge-Transfer Reaction at the Platinum Electrode in Dye-Sensitized Solar Cells. *Electrochim. Acta* **2001**, *46*, 3457-3466.

(145) Norton, J. D.; White, H. S.; Feldberg, S. W.: Effect of the Electrical Double Layer on Voltammetry at Microelectrodes. *J. Phys. Chem* **1990**, *94*, 6772-6780.

(146) Watkins, J. J.; White, H. S.: The Role of the Electrical Double Layer and Ion Pairing on the Electrochemical Oxidation of Hexachloroiridate (III) at Pt Electrodes of Nanometer Dimensions. *Langmuir* **2004**, *20*, 5474-5483.

(147) Sastry, N. V.; Valand, M. K.: Densities, Viscosities, and Relative Permittivities for Pentane+ 1-Alcohols (C1 to C12) at 298.15 K. *J. Chem. Eng. Data* **1998**, *43*, 152-157.

(148) Gadogbe, M.; Chen, M.; Saebo, S.; Beard, D. J.; Zhang, D.: Can Para-Aryl-Dithiols Cross-Link Two Plasmonic Noble Nanoparticles as Monolayer Dithiolate Spacers? *J. Phys. Chem. C* **2015**, *119*, 6626-6633.

(149) Gadogbe, M.; Zhou, Y.; Alahakoon, S. H.; Perera, G. S.; Zou, S.; Pittman Jr, C. U.; Zhang, D.: Structures and Conformations of Alkanedithiols on Gold and Silver Nanoparticles in Water. *J. Phys. Chem. C* **2015**, *119*, 18414-18421.

(150) Bensebaa, F.; Zhou, Y.; Brolo, A.; Irish, D.; Deslandes, Y.; Kruus, E.; Ellis, T.: Raman Characterization of Metal-Alkanethiolates. *Spectrochim. Acta A: Mole. Biomol. Spec.* **1999**, *55*, 1229-1236.

(151) Van Wart, H. E.; Lewis, A.; Scheraga, H. A.; Saeva, F. D.: Disulfide Bond Dihedral Angles from Raman Spectroscopy. *Proc. Nat. Acad. Sci.* **1973**, *70*, 2619-2623.

(152) Yu, N.-T.; DeNagel, D. C.; Pruett, P. L.; Kuck, J.: Disulfide Bond Formation in the Eye Lens. *Proc. Nat. Acad. Sci.* **1985**, *82*, 7965-7968.

(153) Park, J.-W.; Shumaker-Parry, J. S.: Strong Resistance of Citrate Anions on Metal Nanoparticles to Desorption Under Thiol Functionalization. *ACS Nano* **2015**, *9*, 1665-1682.

(154) Smith, D. W.: Ionic Hydration Enthalpies. *J. Chem. Edu.* **1977**, *54*, 540.

(155) Stace, A.: Estimating the Hydration Enthalpies of Neutral Alkali Metal Atoms. *J. Phys. Chem. B* **2006**, *110*, 20742-20744.

(156) Fawcett, W. R.: Thermodynamic Parameters for the Solvation of Monatomic Ions in Water. *J. Phys. Chem. B* **1999**, *103*, 11181-11185.

(157) Tissandier, M. D.; Cowen, K. A.; Feng, W. Y.; Gundlach, E.; Cohen, M. H.; Earhart, A. D.; Coe, J. V.; Tuttle, T. R.: The Proton's Absolute Aqueous Enthalpy and Gibbs Free Energy of Solvation from Cluster-Ion Solvation Data. *J. Phys. Chem. A* **1998**, *102*, 7787-7794.